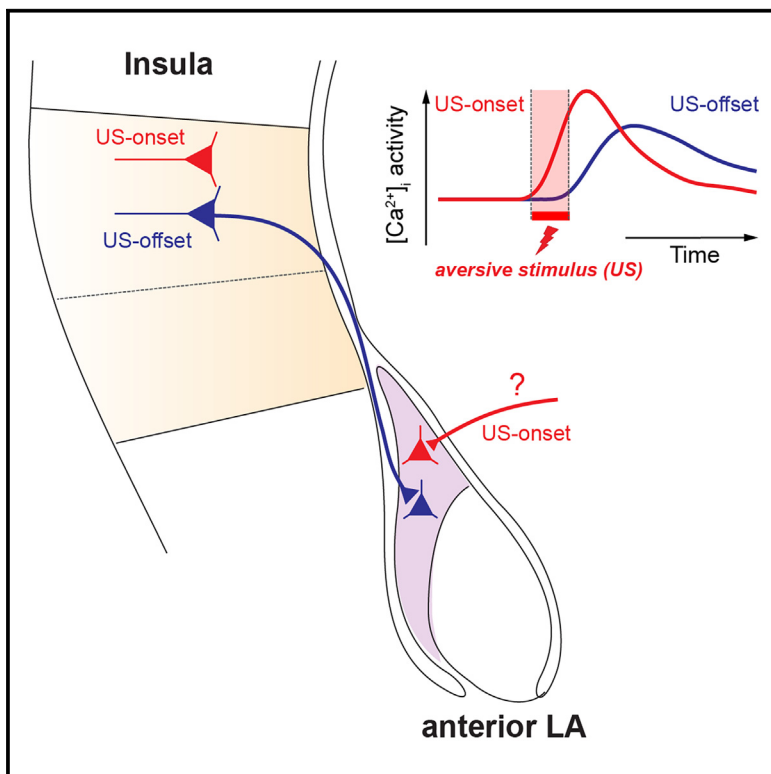


A posterior insula to lateral amygdala pathway transmits US-offset information with a limited role in fear learning

Graphical abstract



Authors

Shriya Palchaudhuri, Bei-Xuan Lin,
Denys Osypenko, Jinyun Wu,
Olexiy Kochubey, Ralf Schneggenburger

Correspondence

ralf.schneggenburger@epfl.ch

In brief

Palchaudhuri et al. show that the posterior insular cortex (pInsCx) codes for aversive footshocks (US) both with onset and offset responses; the US-offset information is selectively transmitted at the pInsCx-to-anterior-LA connection. US-driven activity in this pathway, however, is not necessary for fear learning.

Highlights

- The pInsCx makes a glutamatergic projection that specifically targets the anterior LA
- Separate neuron populations in the pInsCx code for US-onset and US-offset information
- US-offset, but not US-onset, information is transmitted at the pInsCx-to-LA connection
- US-driven activity in the pInsCx-LA network is not necessary for fear learning



Article

A posterior insula to lateral amygdala pathway transmits US-offset information with a limited role in fear learning

Shriya Palchaudhuri,^{1,2} Bei-Xuan Lin,¹ Denys Osypenko,^{1,3} Jinyun Wu,¹ Olexiy Kochubey,¹ and Ralf Schneggenburger^{1,4,*}

¹Laboratory of Synaptic Mechanisms, Brain Mind Institute, School of Life Science, Ecole Polytechnique Fédérale de Lausanne (EPFL), Lausanne, Switzerland

²Neuroscience Institute, New York University Grossman School of Medicine, New York, NY, USA

³Department of Fundamental Neuroscience, University of Lausanne, Lausanne, Switzerland

⁴Lead contact

*Correspondence: ralf.schneggenburger@epfl.ch

<https://doi.org/10.1016/j.celrep.2025.115320>

SUMMARY

During fear learning, associations between a sensory cue (conditioned stimulus, CS) and an aversive stimulus (unconditioned stimulus, US) are formed in specific brain circuits. The lateral amygdala (LA) is involved in CS-US integration; however, US pathways to the LA remain understudied. Here, we investigated whether the posterior insular cortex (pInsCx), a hub for aversive state signaling, transmits US information to the LA during fear learning. We find that the pInsCx makes a robust, glutamatergic projection specifically targeting the anterior LA. *In vivo* Ca²⁺ imaging reveals that neurons in the pInsCx and anterior LA display US-onset and US-offset responses; imaging combined with axon silencing shows that the pInsCx selectively transmits US-offset information to the anterior LA. Optogenetic silencing, however, does not show a role for US-driven activity in the anterior LA or its pInsCx afferents in fear memory formation. Thus, we describe a cortical projection that carries US-offset information to the amygdala with a limited role in fear learning.

INTRODUCTION

Animals and humans must evaluate signs of dangers in their environment and react with appropriate behavior to ensure survival. For this reason, robust mechanisms of aversively motivated associative learning, also called fear learning, have evolved.^{1,2} During this behavior, animals learn to associate an innocuous sensory cue, such as a tone (conditioned stimulus, CS) with a harmful event such as a nociceptive stimulus (unconditioned stimulus, US). Classical work has shown that the amygdala, especially the lateral amygdala (LA), integrates US and CS information.^{2–5} Auditory inputs to the amygdala have been characterized comparatively well, showing that non-lemniscal auditory thalamic nuclei^{6,7} and ventral, higher-order areas of the auditory cortex^{8–10} project with excitatory glutamatergic synapses to the LA. Moreover, it has been shown that long-term plasticity at these inputs is involved in auditory-cued fear learning.^{11–15}

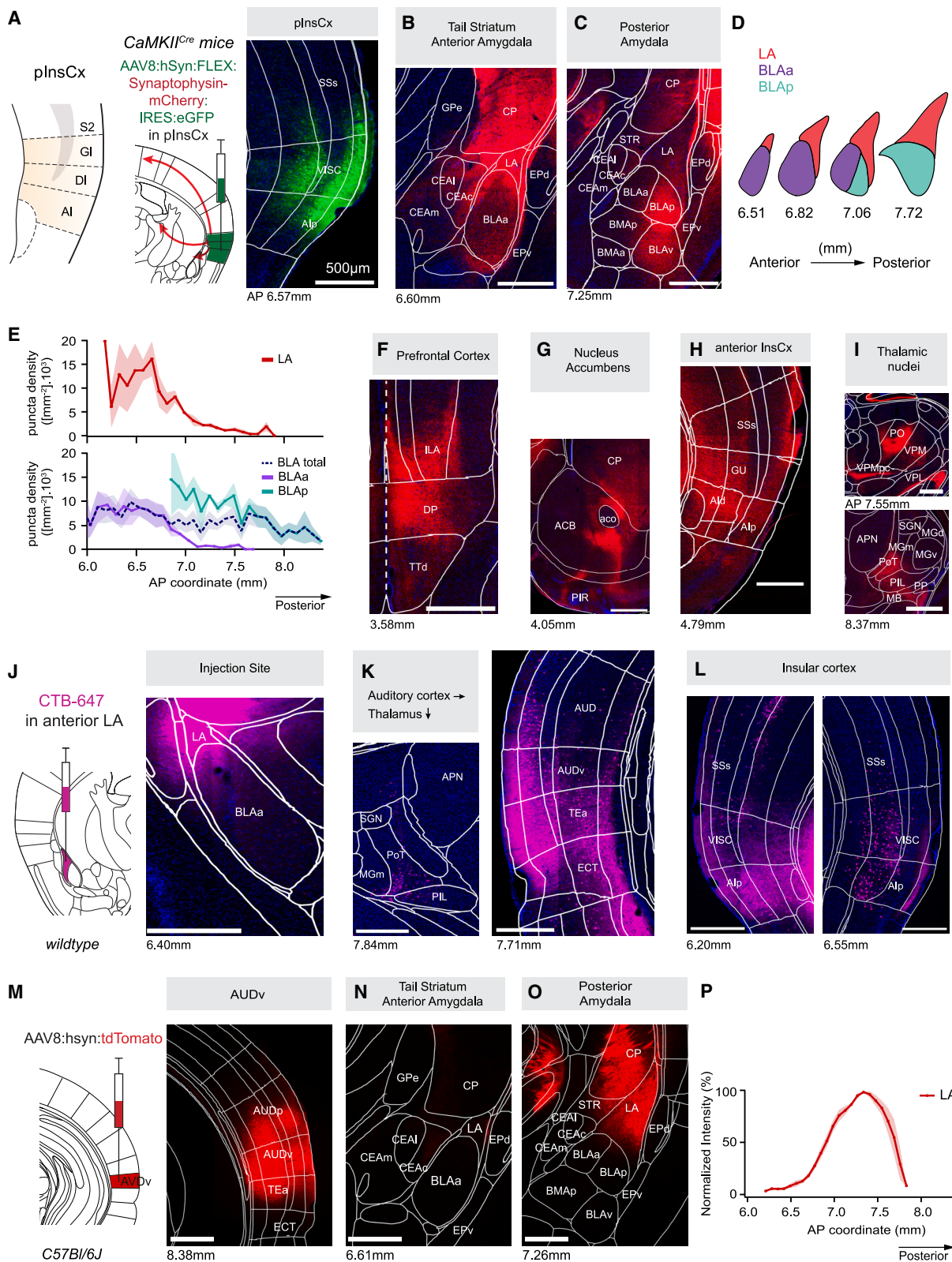
Despite the above findings, the synaptic inputs that cause action potential (AP) firing of LA neurons in response to footshocks, and that therefore drive associative plasticity in the LA,¹⁶ have received little attention. Subpopulations of LA neurons are activated by footshocks.^{5,17,18} In common plasticity models for fear learning, US-driven AP firing of LA principal neurons is regarded as an important factor for the induction of associative synaptic plasticity^{19–21}; in addition, there is notable evidence

for a role of neuromodulators in this process.^{22–24} Nevertheless, the afferent, presumably glutamatergic synapses that carry US information to the LA remain largely unknown, although recent studies have shown that the inputs from the non-lemniscal auditory thalamus can carry US information as well.^{7,25}

The insular cortex has received increased attention as a brain area involved in aversive-state coding, valence processing, fear learning, and fear extinction.^{26–33} This cortical area is located ventral to the motor and somatosensory areas and can be subdivided into anterior, middle, and posterior parts.³⁴ Earlier studies found that the posterior insular cortex (pInsCx) codes for nociceptive stimuli in humans^{35,36} and rats,³⁷ and a recent study has shown that the pInsCx codes for skin temperature.^{38,39} The pInsCx has also been shown to serve as a hub for aversively motivated adaptive behaviors^{26,27,30} (but see Nicolas et al.^{26–33}). Furthermore, the pInsCx processes interoceptive information from the body,⁴⁰ feedback from which has been shown to regulate the extinction of fear memories.²⁷

Regarding the output projections via which the insula might regulate emotional behaviors, a projection from the insula to the central amygdala is well established.^{26,32,41,42} This projection is involved in feeding and drinking behavior,^{31,43,44} in learned taste aversion,^{32,33} in the expression of learned fear,^{28,30} and in anxiety-related behaviors.²⁶ Other recent studies have identified outputs from the pInsCx to the posterior (tail) striatum^{45,46} and have shown that direct- and indirect-pathway neurons in the





(legend on next page)

tail striatum differentially regulate the expression of learned fear.⁴⁶ In addition, a projection from the pInsCx to the LA was found in earlier work in rats and monkeys.^{9,47,48} However, much less is known about the latter projection, and a recent large-scale anatomical study of the inputs and outputs of the mouse insular cortex reported limited evidence for a pInsCx-to-LA connection.⁴²

Based on the role of the pInsCx in the processing of nociceptive information and aversive-state coding,^{26,37} we have addressed the question of whether the pInsCx makes a connection to the LA and, if so, whether this connection transmits US information to the LA that is relevant for fear learning. Circuit mapping and *ex vivo* optogenetics reveal a robust excitatory connection from the pInsCx that specifically targets the anterior LA. *In vivo* Ca²⁺ imaging showed that both brain areas contain neuron pools that code for the start and the end of aversive footshock stimulation (US-onset and US-offset responses, respectively). Imaging combined with optogenetic silencing of afferent axons then revealed that the pInsCx selectively transmits US-offset, but not US-onset, information to the anterior LA. Optogenetic silencing experiments show, however, that US-driven activity in the anterior LA, or at the connection from the pInsCx to the anterior LA, is not necessary for fear memory formation. Our study characterizes a novel pathway from the insula to an amygdalar subregion but finds that this pathway is not involved in transmitting a US-related teaching signal for fear memory formation to the amygdala.

RESULTS

Anatomical evidence for a pInsCx-to-LA connection

We hypothesized that the pInsCx sends information about aversive footshocks to downstream brain areas involved in fear learning, including the LA. Therefore, we started by investigating the output connections of the pInsCx, using a virus-mediated anterograde labeling approach. The insular cortex is subdivided, from dorsal to ventral, into granular, dysgranular, and agranular

areas (Figure 1A, left). We mainly targeted the granular and dysgranular areas in the pInsCx (pInsCx-GI and -DI), which together are called the visceral cortex in the Allen Brain Atlas (ABA)⁴⁹ (“VISC”; Figure 1A, right). To validate the delineation of the dorsoventral location of the pInsCx in the ABA, we used two transgenic Cre mouse lines for relevant marker genes (Figures S1A and S1B). First, we used the Scnn1a^{Cre} × tdT mouse line to label layer 4 neurons in the cortex.⁵⁰ This showed that the cortical layer 4 ended ventrally at the pInsCx-S2 border (Figure S1A; see also Bokiniec et al.³⁹). Second, we employed the Etv1^{CreERT2} × tdT mouse line to label layer 5a neurons.⁵¹ This revealed clear labeling of layer 5a in the primary (S1) and secondary (S2) somatosensory cortex. Interestingly, the band of Etv1-expressing neurons expanded in width more ventrally in the pInsCx-GI and -DI, correlating with the thinning of layer 4 in the pInsCx-DI (Figure S1B). These findings confirm that in alignments of brain sections to the ABA, we can correctly assign the dorsoventral location of the insular cortex.

We next performed anterograde labeling from the pInsCx-GI and -DI, using a viral vector with an mCherry-synaptophysin fusion construct to label distant nerve terminals and cytosolic eGFP to label the injection site (AAV8:hSyn:FLEX: synaptophysin-mCherry-IRES-eGFP; see STAR Methods). This vector was injected into the right pInsCx of CaMKII^{Cre} mice to target the expression to principal neurons ($N = 3$ mice). The results revealed mCherry-labeled axons in the tail striatum (labeled CP in the figures; see also Kintscher et al.⁴⁶), amygdala-striatal transition zone, and anterior LA (Figure 1B), as well as in the posterior basolateral amygdalar nucleus (BLAp, Figure 1C; note that this structure is sometimes referred to as lateral BA) and weaker outputs in the central amygdala (CeA, Figure 1B; see Table S1 for brain-area abbreviations). Because we were most interested in the outputs to the BLA complex, we next analyzed the nerve-terminal density along the anterior-posterior axis in three substructures of this brain area: The LA, anterior BLA (BLAa), and BLAp (Figure 1D). We found a high nerve-terminal density in the anterior LA, which notably decreased in the posterior LA (Figure 1E,

Figure 1. Anatomical evidence for a pInsCx-to-LA connection

Brain section images were aligned to the Allen Mouse Brain Atlas (see STAR Methods); numbers below each image panel give the anterior-posterior position according to the reference atlas. Abbreviations of brain areas follow the reference atlas and are given in Table S1.

(A) Left: scheme of the experimental approach for anterograde labeling of pInsCx projections. Right: eGFP fluorescence image of the injection site. The images in (A)–(I) and Figures S1C and S1D are from one representative mouse.

(B and C) Example images showing synaptophysin-mCherry fluorescence in the tail striatum (labeled “CP”) and anterior LA (B), and in the more posteriorly located BLAp (C).

(D) Outlines of the Allen Mouse Brain Atlas areas of the BLA complex.

(E) Analysis of the density of nerve terminals from the pInsCx in three BLA substructures along the a-p axis, i.e., in the LA (top) and in the basal amygdala (BA) structures BLAa and BLAp (bottom). Each trace is an average ± SEM of $N = 3$ mice.

(F–I) Synaptophysin-mCherry fluorescence in the ventral prefrontal cortex (F), the nucleus accumbens (G), the anterior insula (H), and various thalamic nuclei (I).

(J) Experimental approach for retrograde labeling experiments (left) and example image of a CTB-647 injection into the anterior LA (right). The images in (J)–(L) and in Figure S1E are from a representative mouse. Similar observations were made in a total of $N = 3$ mice.

(K) Example images showing retrogradely labeled cells in the posterior thalamic nucleus (left), and ventral auditory cortex and TEa (right).

(L) Retrogradely labeled cells in the ipsilateral (left) and contralateral pInsCx (right). See also Figure S1 and Table S1.

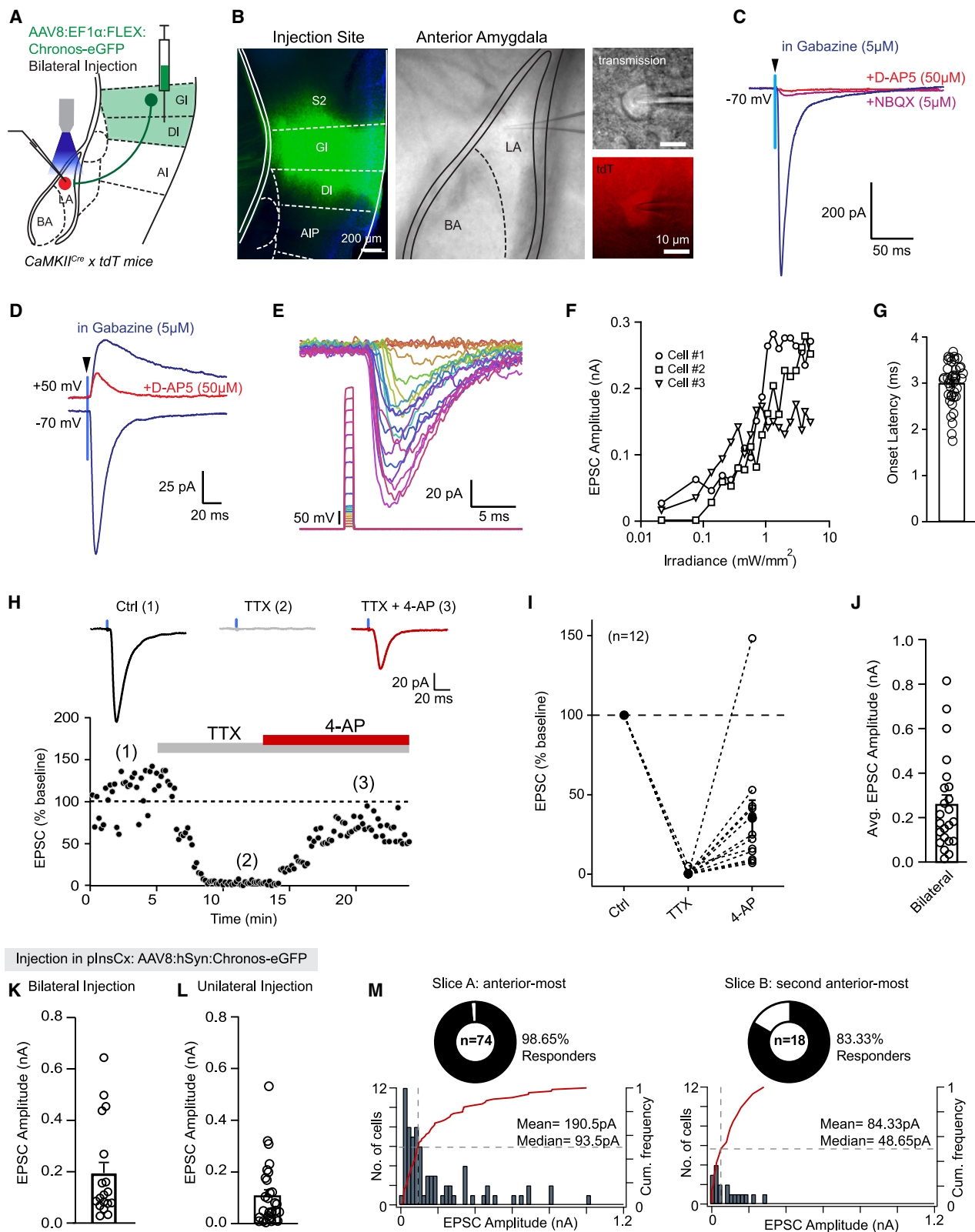
(M) Experimental approach for complementary anterograde labeling from the ventral auditory cortex (AUDv, left), and representative image of a virus injection site (right).

(N) Output axons from the AUDv are largely absent on the level of the anterior LA (compare to B).

(O) Output axons from the AUDv, indicated by tdTomato fluorescence, innervating the posterior LA and the adjacent VTS (labeled “CP”).

(P) Quantification of tdTomato fluorescence along the a-p axis of the LA (average ± SEM from $N = 3$ mice). Note that AUDv output axons target the posterior LA, as opposed to axons from the pInsCx (compare with E [top]).

Scale bars, 500 μm. In (E) and (P), traces in full colors and hue are mean ± SEM. See also Figure S1 and Table S1.



(legend on next page)

red data trace; $N = 3$ mice). A weaker projection was observed in the BLAA (Figure 1E, violet data trace), whereas the BLAp was densely innervated by the pInsCx (Figures 1C and 1E, cyan data trace; $N = 3$ mice). In addition to the innervation of the BLA complex by the pInsCx, we observed nerve terminals in other forebrain areas, including the infralimbic and dorsal peduncular areas of the ventral prefrontal cortex (ILA and DP, Figure 1F; Yasui et al.⁵²), nucleus accumbens (ACB) (Figure 1G; Gehrlach et al.²⁶; Wang et al.^{28,30}), anterior insular cortex (Figure 1H; Kimura et al.⁵³), and thalamic nuclei such as the posterior complex of thalamus (PO),³⁹ posterior triangular thalamic nucleus (PoT),⁵⁴ ventral posteromedial nucleus of thalamus (parvicellular part) (VPMpc),^{55,56} and medial geniculate complex, medial part (MGm)/posterior intralaminar thalamic nucleus (PIL) (Figure 1I). Some of these thalamic structures, such as the PO, PoT, and the PIL, are target areas of the spinothalamic pathway and/or have been associated with coding aversive information.^{57,58} Furthermore, the agreement of the output structures observed here with previous literature suggests that we correctly targeted the pInsCx. Notable mCherry expression was also observed in some contralateral brain areas such as the anterior LA, the tail striatum, and the pInsCx (Figures S1C and S1D). Taken together, anterograde tracing reveals dense output of the pInsCx to the BLA complex, which mainly targets the anterior LA and the BLAp. Furthermore, anterograde labeling reveals additional characteristic outputs of the pInsCx to other forebrain areas.

We next validated the anatomical finding of a pInsCx-to-LA projection using retrograde labeling. We injected CTB-647 into the anterior LA (Figure 1J), because as we found above, this area receives dense axonal input from the pInsCx. Back-labeled cells were observed in the contralateral BLAA and ventral BLA (BLAv) (Figure S1E), PoT (Figure 1K), ventral auditory cortex (AUDv), temporal association area (TEa), and ecto-rhinal area (ECT) (Figure 1K), as well as in the ipsi- and contralateral pInsCx (Figure 1L). Targeting of the contralateral

posterior LA with CTB-488 in the same mouse (Figure S1F) led to a differential back-labeling, with fewer cells in the pInsCx and the PoT, whereas back-labeled cells were now found in the MGm, in agreement with previous studies.⁷ The AUDv and the TEa^{8,10} were also back-labeled, as we found for the anterior LA (Figures S1G and S1H). In a further experiment, we performed anterograde labeling from the AUDv, which revealed output axons in the posterior LA but less so in the anterior LA, a pattern complementary to the one observed for the projection from the pInsCx (Figures 1M–1P; $N = 3$ mice). Taken together, antero- and retrograde tracing establish an anatomical projection from the pInsCx to the anterior LA and the BLAp. This newly defined pInsCx-to-LA connection targets more anterior regions in the LA than the AUDv.

The pInsCx makes a robust glutamatergic connection with the LA

To validate whether the anatomically defined projection from the pInsCx to the anterior LA represents a functional glutamatergic connection as we expect, we employed optogenetically assisted circuit mapping.⁵⁹ We expressed the channelrhodopsin variant Chronos⁶⁰ in principal neurons of the pInsCx on both brain sides, using CamKII^{Cre} × tdT mice and a Cre-dependent expression vector (Figure 2A and STAR Methods). Four to five weeks later, we performed whole-cell recordings of principal neurons in the anterior LA using tdTomato fluorescence to select CamKII^{Cre}-positive principal neurons in the LA for recordings (Figure 2B, right). Single blue-light pulses (470 nm; ~5 mW/mm² intensity) caused optogenetically evoked excitatory postsynaptic potentials (EPSCs) with a fast, NBQX-sensitive component at negative holding potentials (~70 mV; Figure 2C) and an additional slow component at +50 mV; the latter was blocked by the NMDA antagonist D-AP5 (D,L-2-amino-5-phosphonovaleric acid, 50 μM; Figure 2D). These experiments show that the pInsCx-LA connection is a glutamatergic synapse.

Figure 2. Optogenetic circuit mapping reveals a robust glutamatergic synapse from the pInsCx to the LA

- (A) Scheme of the experimental design.
- (B) Post hoc validation of Chronos-eGFP expression at the injection site in the pInsCx (left) and image of the recording site in the LA slice (middle), as well as zoom-ins of a recorded tdTomato-positive LA principal neuron (right).
- (C) Example of an optogenetically evoked EPSC at ~70 mV (blue trace; in the presence of 5 μM gabazine to block feedforward inhibition). Addition of 5 μM NBQX blocked the fast AMPA-EPSC (maroon trace), and the remaining minimal NMDA-EPSC was further blocked after the addition of 50 μM D-AP5 (red trace).
- (D) Optogenetically evoked EPSC at ~70 mV, and a mixed fast and slow EPSC at +50 mV (blue traces; in the presence of 5 μM gabazine). Addition of 50 μM D-AP5 blocked the slow NMDA-EPSC component at +50 mV (red trace).
- (E) Gradually increasing the stimulus light intensity led to a gradual increase of optogenetically evoked EPSCs.
- (F) Input-output relationship of EPSCs as a function of light intensity ($n = 3$ example recordings).
- (G) Individual and average data for onset latency of optogenetically evoked EPSCs ($n = 40$ recordings from $N = 10$ mice).
- (H) Time plot of optogenetically evoked EPSC amplitudes in an example recording upon 1-ms light stimulation under control conditions (1), after application of 1 μM tetrodotoxin (TTX) (2), and after co-application of a 4-AP (1 mM) in the continued presence of TTX (3).
- (I) Quantification of average optogenetically evoked EPSC amplitudes under the three conditions as in (H) ($n = 12$ recordings from $N = 5$ mice). Note the partial recovery of the EPSC amplitudes after application of 4-AP in the continued presence of TTX.
- (J) Average and individual data points for optogenetically evoked EPSC amplitudes recorded after bilateral, Cre-dependent expression of Chronos in CamKII^{Cre} × tdT mice (see A; $n = 23$ recordings from $N = 6$ mice).
- (K) Average and individual data points for optogenetically evoked EPSC amplitudes recorded after bilateral, Cre-independent expression of Chronos in CamKII^{Cre} × tdT mice (AAV vector as indicated; $n = 18$ recordings from $N = 4$ mice).
- (L) Average and individual data points for optogenetically evoked EPSC amplitudes recorded after unilateral Cre-independent expression of Chronos ($n = 29$ recordings from $N = 10$ mice).
- (M) Connection probability and distribution of optogenetically evoked EPSC amplitude for the anteriormost slice (left) and the second-anteriormost slice on the level of the LA (right). A significantly higher connection probability and a trend of larger EPSC amplitudes in the anteriormost slice as compared to the second-anteriormost slice was revealed (see results for statistical parameters).

Scale bars, 200 μm (B, left) and 10 μm (B, right). In (G) and (I)–(L), error bars indicate SEM. In (C) and (D), average traces are from $n = 10$ subsequent EPSCs.

We next measured input-output relations by varying the intensity of the stimulus light to study the convergence of presynaptic axons onto LA principal neurons (see also Litvina and Chen^{61,62} and Gjoni et al.^{61,62}). Increasing the light intensity gradually increased the EPSC amplitudes without discernible steps, indicating that the compound EPSCs were composed of multiple unitary EPSCs with smaller amplitudes (Figures 2E and 2F). The EPSCs had a fast onset latency (3.0 ± 0.07 ms, $n = 40$ recordings; Figure 2G) and were blocked by tetrodotoxin (TTX, 1 μ M). The block was partially recovered by adding the K⁺-channel blocker 4-aminopyridine (4-AP, 1 mM; $n = 12$ recordings; Figures 2H and 2I). Together, these findings show that principal neurons in the pInsCx make a direct, monosynaptic connection onto principal neurons in the LA.

The average EPSC amplitude upon near-maximal light intensity was 257 ± 44 pA (Figure 2J; $n = 23$ recordings from $N = 6$ mice with bilateral, Cre-dependent expression of Chronos). We performed additional experiments to corroborate these results and to further explore the nature of the presynaptic neurons in the pInsCx that innervate the LA. First, using a Cre-independent vector to drive the expression of Chronos bilaterally in the pInsCx (AAV8:hSyn:Chronos-eGFP), we found EPSCs of indistinguishable amplitudes (Figure 2K, compare to Figure 2J; $p = 0.1468$, $U = 151$, Mann-Whitney U test). Second, unilateral expression of Chronos led to smaller EPSCs as compared to bilateral expression (Figure 2L, $p = 0.0495$, $U = 171$, Mann-Whitney U test). This result agrees with our anatomical finding that the LA receives axons from both the ipsi- and the contralateral pInsCx (Figure 1). Finally, we found a larger connectivity and a trend toward larger EPSC amplitudes in the anteriormost slices of the LA as compared to the subsequent, second-anteriormost slice (Figure 2M; for connectivity: $p = 0.022$, Fisher's exact test; for EPSC amplitudes: $p = 0.052$, $U = 468.5$, Mann-Whitney U test). This result recapitulates the anatomical finding that pInsCx axons preferentially innervate the anterior LA (Figure 1). Taken together, optogenetically assisted circuit mapping reveals a robust glutamatergic connection between the pInsCx and the anterior LA.

In vivo Ca²⁺ imaging reveals separate neuron pools with US-onset and US-offset coding

We have shown that the pInsCx projects to the anterior LA, where it makes a robust excitatory synaptic connection with principal neurons (Figures 1 and 2). We next investigated how principal neurons in the pInsCx code for footshock information by performing *in vivo* Ca²⁺ imaging with a miniature microscope⁶³ in freely behaving mice during fear learning. We expressed the Ca²⁺ sensor GCaMP6m unilaterally in the left pInsCx in a Cre-dependent manner in CaMKII^{Cre} mice and implanted a GRIN lens over the pInsCx in the same surgery (Figure 3A). Four weeks later, the mice underwent auditory-cued fear learning during which, in a training session, six trains of tone beeps (CS) terminated with a 1-s-long footshock (US; see STAR Methods and Figure 3B). Post hoc histological validations showed that most of the imaged neurons were located within the pInsCx-GI and -DI (Figures 3C–3E, “VISC”). Neurons located in the adjacent S2 or agranular insular cortex were excluded from the analysis (Figure 3E, supplemental somatosensory area [SSs] and posterior agranular insular area [Alp], respectively).

Ca²⁺ imaging in the pInsCx during each session of the fear-learning protocol revealed that a moderate proportion of CamKII⁺ principal neurons responded with a short-latency Ca²⁺ increase to footshocks (45 out of 175, or 25.7% of the imaged neurons, $N = 7$ mice; Figures 3F and 3G). Interestingly, there were also neurons that responded with longer latencies to footshocks (Figure 3F, arrows). When adapting the sorting criterion to account for these delayed responses, we found that a subpopulation of neurons (10.3%) responded with late-onset responses to footshock stimulation (“US-offset” response, Figures 3I–3K). Furthermore, we found smaller populations of principal neurons that responded with a decrease in Ca²⁺ either to the onset or to the offset of the footshock stimuli (Figures 3G and 3J, blue traces; 7.4% and 7.4% of the imaged neurons for each response type). The amplitude of the Ca²⁺ responses did not significantly vary across the six footshock presentations for neither of the four response types (Figures 3H and 3K; see figure legend for statistical test values). Plotting the onset latencies of Ca²⁺ responses revealed a first peak in the distribution at ~ 200 ms representing the US-onset responses, followed by events with longer latencies (Figure 3L), consistent with the separation of events into US-onset and -offset classes. Taken together, *in vivo* Ca²⁺ imaging shows that a subpopulation of principal neurons in the pInsCx becomes activated at the onset of aversive footshock stimulation. Furthermore, a separate subpopulation of pInsCx principal neurons responds after the footshocks (US-offset response) and thereby likely codes for the end of aversive stimulation, which is an unexpected finding.

The pInsCx drives US-offset but not US-onset responses in the anterior LA

We found that separate subpopulations of pInsCx principal neurons show US-onset and US-offset responses during fear learning (Figure 3). Because the pInsCx makes a robust glutamatergic projection to the anterior LA, we next investigated whether information about footshocks is transmitted at this synaptic connection. For this purpose, we performed *in vivo* Ca²⁺ imaging in the anterior LA combined with optogenetic inhibition of axons arising from the pInsCx, employing a dual-wavelength miniature microscope.⁶⁴

We expressed GCaMP6m in a Cre-dependent manner in the left anterior LA of CamKII^{Cre} mice (AAV8:hSyn:FLEX:GCaMP6m) and halorhodopsin bilaterally in the pInsCx (AAV8:hSyn:eNpHR3.0-eYFP). In the same surgery, a GRIN lens was implanted over the left anterior LA (Figure 4A). Five weeks later, we imaged neurons in the anterior LA during each session of an auditory-cued fear-learning protocol (Figure 4B). Post hoc rendering of the positions of imaged neurons overlaid on the 3D space of the ABA showed that $\sim 40\%$ of all imaged neurons were located in the LA; these neurons were further analyzed (Figures 4C and 4D, red dots). During the training session, mice were presented with six paired CS-US presentations. We applied brief (3 s) pulses of orange light during the first, third, and fifth footshocks to activate halorhodopsin, whereas the other US presentations were used as internal controls (Figures 4B and S2B). As an additional control, a group of mice received an injection of PBS bilaterally into the pInsCx instead of the halorhodopsin vector (Figures 4A and 4B).

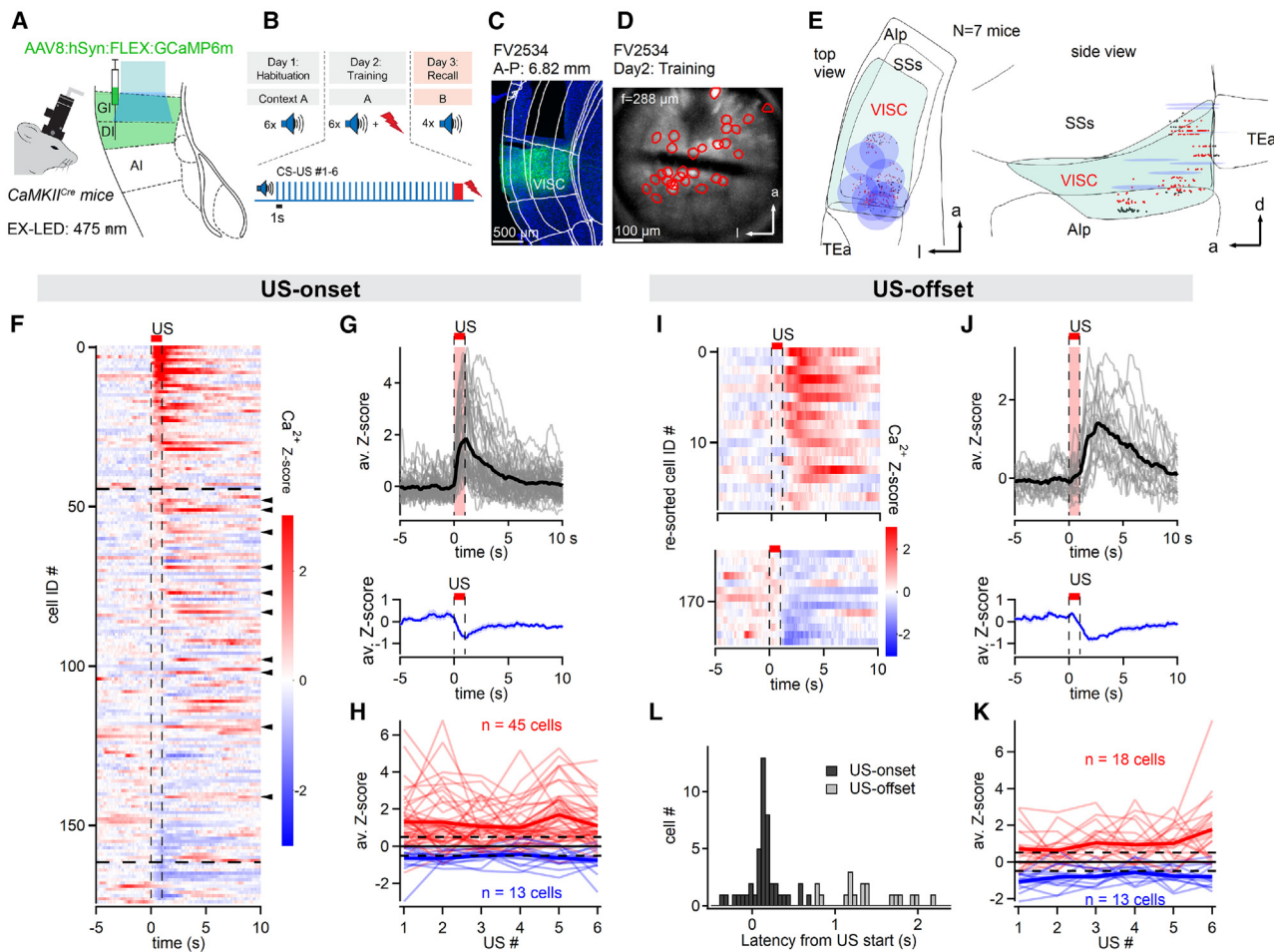


Figure 3. *In vivo* Ca^{2+} imaging of plnsCx principal neurons reveals onset as well as offset responses to footshocks

(A and B) Scheme of the experimental design of GCaMP6m-based *in vivo* Ca^{2+} imaging of plnsCx neurons during fear learning.

(C) Post hoc histological validation of GCaMP6m expression and GRIN lens positioning in the plnsCx.

(D) Maximal-intensity projection images of GCaMP6m fluorescence at a focal plane of 288 μm overlaid with detected ROIs (red circles) in an example mouse. (E) 3D reconstructions of imaged neurons (red and black dots) and the GRIN lenses (blue disks) aligned to ABA coordinates (see STAR Methods). Only neurons located within the plnsCx-GI and -DI ("VISC") were maintained for the final analysis (red dots).

(F) Raster plot showing Z-scored Ca^{2+} traces of all recorded cells ($n = 175$ cells in $N = 7$ mice) sorted by their average Ca^{2+} response during footshocks ("US-onset" responses; top red bar indicates 1-s footshock occurrence). Upper and lower dashed lines show limits for positive and negative responses to footshocks, respectively. Black arrowheads indicate example neurons with US-offset response (see I–K).

(G) Ca^{2+} traces of neurons with a positive (top) and a negative (bottom) US-onset response. Each trace is the average across the six footshock presentations. For the positive responders, traces from individual neurons were overlaid (gray).

(H) Neither the positive nor the negative responses with US-onset characteristics (red and blue data, respectively) showed a significant dependence on time with repeated footshocks ($p = 0.178$ and $p = 0.455$, Friedman test).

(I) Raster plot showing Z-scored Ca^{2+} traces of cells re-sorted by their average response to a time after footshock (US-offset responses, see STAR Methods). There were neurons with positive (top) and negative (bottom) US-offset responses. Cell IDs correspond to the re-sorted order.

(J) Average Ca^{2+} traces of neurons with a positive (top) and a negative (bottom) US-offset response. Each trace is the average across six footshock presentations. For the positive responders, traces from individual neurons were overlaid (gray).

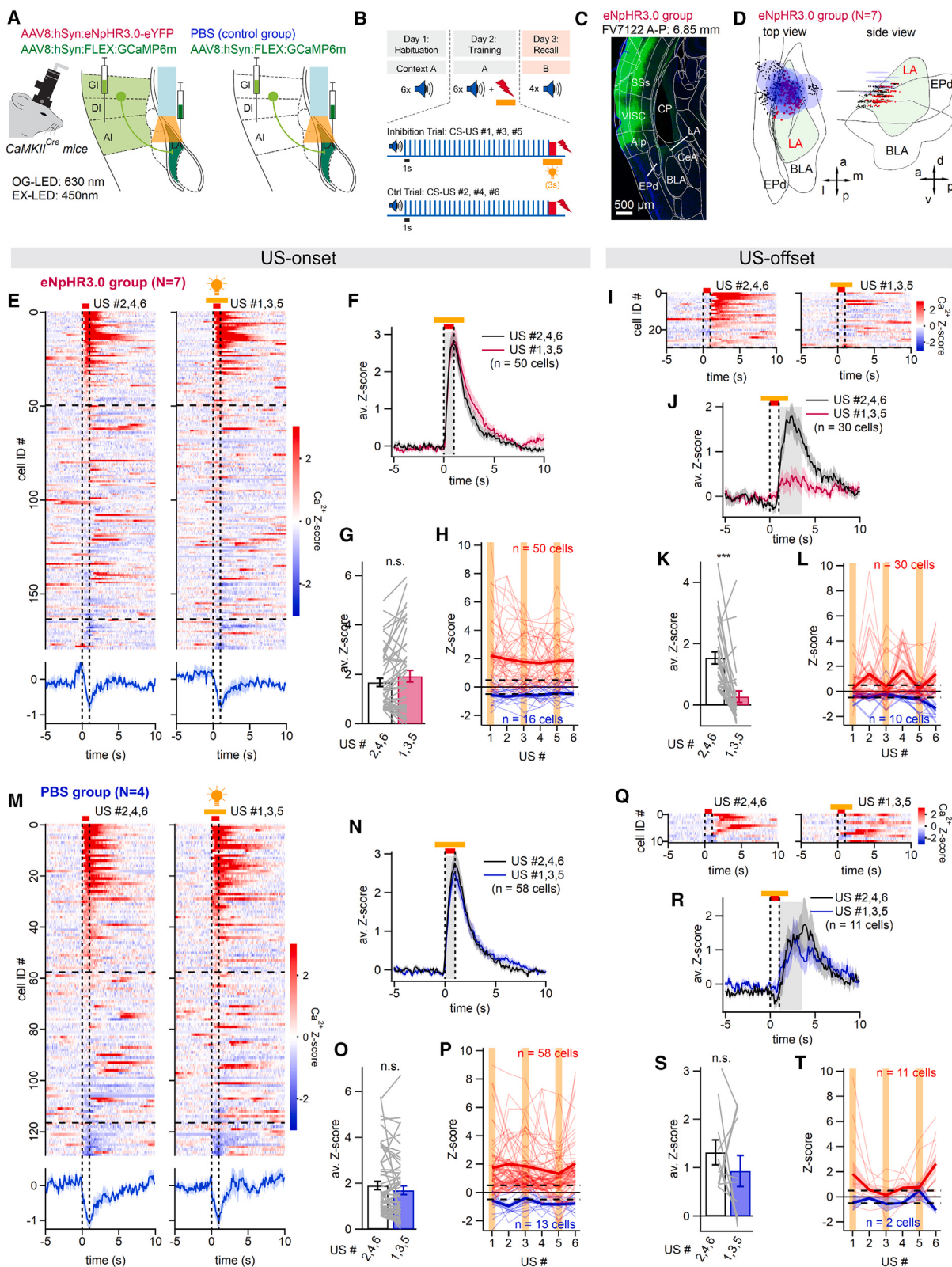
(K) Neither the positive nor the negative responses with US-offset characteristics (red and blue data, respectively) showed a significant dependence on time with repeated footshocks ($p = 0.274$ and $p = 0.301$, Friedman test and one-way repeated-measures ANOVA, respectively).

(L) Histogram of onset latency of US-onset and US-offset responses.

Scale bars, 500 μm (C) and 100 μm (D). In (G), (H), (J), and (K), thick lines represent average traces. In (G [bottom]) and (J [bottom]), data traces and light-color hues indicate mean \pm SEM.

During auditory-cued fear learning, mice showed increasing levels of freezing during the training session; upon fear memory recall, mice responded with increased freezing to the CS, indicating that they had formed an auditory-cued fear memory

(Figures S2A–S2F). In both the halorhodopsin and the PBS groups ($N = 7$ and $N = 4$ mice), we found that footshocks led to Ca^{2+} responses in a subpopulation of neurons. As in the plnsCx, the responses could be separated according to their onset



(legend on next page)

latency. Thus, 27.8%, and 44.6% of neurons in the halorhodopsin and the PBS group, respectively, showed US-onset responses (Figures 4E, 4F, 4M, and 4N). On the other hand, 16.7% and 8.5% of the neurons in the halorhodopsin group and the PBS group, respectively, showed US-offset responses (Figures 4I–4L and 4Q–4T).

In the halorhodopsin group, application of brief, 3-s orange-light pulses did not lead to significant changes in the amplitude of the US-onset responses as compared to the footshock responses without light (Figure 4G, $p = 0.265$, Wilcoxon test; Figure 4H, $p = 0.4996$, $F_{1,49} = 0.4627$, two-way repeated measures [RM] ANOVA). In the PBS group, as expected, orange light also had no effect on the US-onset responses (Figures 4M–4P, $p = 0.190$, Wilcoxon test). Intriguingly, however, light pulses suppressed the US-offset responses in the halorhodopsin group (Figure 4K; $p < 0.0001$, Wilcoxon test; Figure 4L, $p < 0.0001$, $F_{1,29} = 26.03$, two-way RM ANOVA). As expected, in the PBS group orange light did not change the US-offset responses (Figure 4S; $p = 0.365$, Wilcoxon test). These experiments show, first, that a substantial percentage of neurons in the anterior LA show a US-onset response to footshock stimulation, and second, that a smaller subpopulation of neurons responds with a longer latency to footshocks, similar to what we observed in the pInsCx (US-offset responses). Third, the US-offset responses in the anterior LA are transmitted at the pInsCx-to-anterior-LA connection, as these responses were significantly suppressed by optogenetic silencing of axons arising from the pInsCx.

We also analyzed the responses of neurons in the anterior LA to the auditory stimuli (CS) across the duration of the fear-learning experiments, using the data from the PBS group (Figures S2G–S2L). This suggests that neurons of the anterior LA code for the CS in a plastic manner, perhaps similar to CS-driven activity found in other regions of the BLA complex.^{5,18} Nevertheless, the exact form(s) of CS plasticity in neurons of the anterior LA during fear learning, and a more informed comparison to previous data obtained in the BLA, must await future studies.

Transmission of US-offset information at the pInsCx-to-LA projection is not necessary for auditory-cued fear learning

Using *in vivo* Ca²⁺ imaging combined with axon silencing, we found evidence for transmission of US-offset, but not of US-onset, information at the pInsCx-to-anterior-LA connection (Figure 4). Therefore, we next investigated whether US transmission at this connection has detectable behavioral roles in auditory-cued fear learning. We initially experimented with an AAVretro-based approach, in an attempt to specifically target LA projectors in the pInsCx. We found, however, that co-infusion of AAVretro:Cre and CTB-647 into the LA did not lead to a strong overlap of back-labeled and Cre-expressing neurons in the pInsCx. Furthermore, Cre-expressing neurons had axonal outputs to many of the projection targets of the pInsCx revealed in Figure 1 (Figure S3). These findings indicate a methodological limitation of the AAVretro approach at this projection and/or a high level of axon collateralization of pInsCx principal neurons.

We therefore employed an approach based on silencing of the pInsCx output axons in the anterior LA. We expressed halorhodopsin bilaterally in the pInsCx of C57Bl/6J mice and placed optic fibers over each anterior LA in the same surgeries (Figures 5A and 5B; $N = 16$ mice). Mice in a control group received a virus driving the expression of eGFP (Figure 5A; $N = 13$ mice). Four weeks later, mice underwent fear learning, and green laser light (wavelength, 561 nm; 10 mW) was applied in a time-locked manner during each of the six footshocks (Figure 5C). As we showed with *in vivo* Ca²⁺ imaging, this optogenetic silencing protocol leads to the suppression of the US-offset responses in the anterior LA (Figure 4). Of the 16 mice in the halorhodopsin group, it was necessary to exclude 8 mice from the analysis because of misplacements of optic fibers in at least one hemisphere ($N = 6$) or because of insufficient expression of halorhodopsin on at least one brain side ($N = 2$) (see Figure S4 for the histological validations).

Figure 4. The pInsCx drives US-offset, but not US-onset, responses in the anterior LA

- (A) Scheme of *in vivo* Ca²⁺ imaging in the LA with GCaMP6m and simultaneous optogenetic inhibition of input axons from the pInsCx (left) and approach for control mice (right).
- (B) Experimental strategy of optogenetic silencing during the first, third, and fifth footshock presentation of the training session.
- (C) Post hoc histological validation of GCaMP6m and eNpHR3.0-eYFP expression, and placement of the GRIN lens over the anterior LA in an example mouse.
- (D) 3D reconstructions of imaged neurons and the GRIN lenses (blue disks) aligned to ABA coordinates. Neurons located within the anterior LA (red dots) were kept for final analysis; all others (black dots) were not analyzed further.
- (E–K) Data from mice in the halorhodopsin group. (E) (Top) Color-coded plot of Z-scored Ca²⁺ traces for $n = 180$ LA neurons imaged in the halorhodopsin group ($N = 7$ mice), separated for footshocks #2, #4, #6 (no light; left) and for footshocks #1, #3, #5 (with orange light to activate halorhodopsin; right). Data were sorted according to their average US-onset response to US #2, #4, and #6. (Bottom) Average for negative US-onset Ca²⁺ responses (see lower dashed line in top panel). (F) Positive US-onset responses averaged for footshocks #2, #4, #6 (no light; black trace) and for footshocks #1, #3, #5 (with orange light; red trace). (G) Average and individual data points of peak Ca²⁺ amplitudes for US-onset responses with and without orange light (pink and gray data, respectively). (H) Peak Ca²⁺ amplitudes across the six footshock presentations for positive and negative US-onset responses. Note the stability of US-onset responses over time, despite the application of orange light during footshocks #1, #3, and #5 (orange vertical lines). (I–L) The data follow the same logic as stated for (E)–(H), now showing the US-offset responses in anterior LA neurons of the halorhodopsin group. Note the decrease of the US-offset responses during orange light application (J and K, and orange lines in L; see results for statistical parameter values). (M–P) The data follow the same logic as stated in for (E)–(H), now showing the US-onset responses in anterior LA neurons in a separate group of mice injected with PBS into the pInsCx (control group). Note that, as expected, orange light application did not modulate the amplitude of US-onset Ca²⁺ responses (see results for statistical parameter values). (Q–T) The data follow the same logic as stated for (I)–(L), now showing the US-offset responses in the PBS group. Note that orange light application did not modulate the amplitude of US-offset Ca²⁺ responses (see results for statistical parameter values).
- Scale bar in (C), 500 μm. In (E), (F), (H), (I), (L), (M), (N), (P), (R), and (T), data traces and light-color hues indicate mean ± SEM. In (G), (K), (O), and (S), error bars indicate SEM. See also Figure S2.

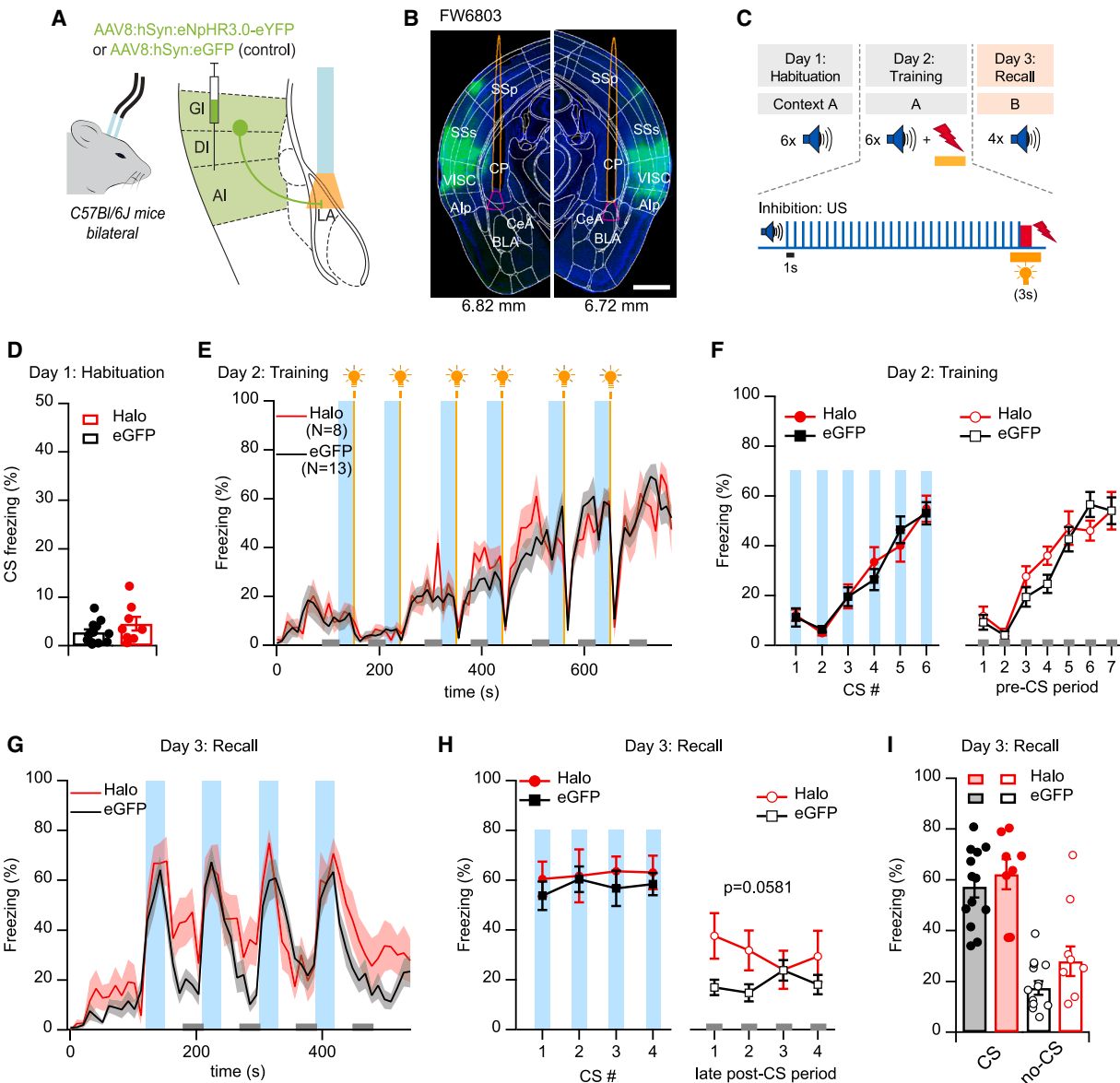


Figure 5. Pathway-specific silencing finds no role for the plnsCx-anterior LA projection in fear memory formation

(A) Scheme of the bilateral expression of halorhodopsin-eYFP (red) or eGFP (control) in the plnsCx and the positioning of optic fiber implants bilaterally above the anterior LA.

(B) Post hoc histological validation of bilateral halorhodopsin-eYFP expression in the plnsCx and optical fiber positioning over the anterior LA in example mouse FW6803 (see also Figure S4 for images from all halorhodopsin mice).

(C) Scheme of the timing of optogenetic inhibition of plnsCx axons, centered on the footshock presentations during the training session.

(D) Average and individual data points for freezing during the CS periods during the habituation session for mice in the halorhodopsin and eGFP groups ($N = 8$ and $N = 13$; red and black data points, respectively).

(E) Time-resolved average freezing behavior for mice in the halorhodopsin and control groups during the training session (red and black traces, $N = 8$ and $N = 13$, respectively). Vertical blue bars indicate the CS; yellow bars indicate the footshock presentations.

(F) Quantification of freezing during the 30-s CS and pre-CS epochs (left and right panels, respectively) during fear memory formation. Freezing during neither the CS nor the pre-CS periods was significantly different between the groups (see results for statistical parameters).

(G) Time-resolved average freezing behavior for mice in the halorhodopsin and control groups during fear memory recall ($N = 8$ and $N = 13$ mice, respectively).

(H) Quantification of freezing during the 30-s CS blocks (left) and during 30-s late post-CS periods (right) during fear memory recall. See results for parameter values for statistical tests.

(I) Average and individual data for freezing during the CS (filled dots and bars) and late post-CS periods (open dots and bars) averaged across the four CS presentations.

Scale bar in B), 1 mm. In (D), (F), (H), and (I), data are mean \pm SEM. In (E) and (G), traces and light-color hues indicate mean \pm SEM. See also Figures S3 and S4.

During the habituation session of the fear-learning protocol, the mice showed little freezing, and, as expected, the amount of freezing was indistinguishable between the halorhodopsin and control groups (Figure 5D; $p = 0.195$, $t_{19} = 1.342$, t test). During the training session, mice in both groups showed a gradual increase in freezing, which was transiently interrupted after each footshock, caused by running of mice immediately following each shock (Figure 5E; blue and yellow lines indicate the CSs and the footshock presentations, respectively). Analyzing the behavior during the CS and during 30-s periods immediately preceding each CS showed that freezing during both periods was unchanged in the halorhodopsin group as compared to the control (eGFP) group (Figure 5F [left] for CS periods: $p = 0.917$, $F_{1,19} = 0.011$; Figure 5F [right] for pre-CS periods: $p = 0.506$, $F_{1,19} = 0.458$; two-way RM ANOVA). Thus, optogenetic inhibition of pInsCx axons in the anterior LA during shock presentation does not lead to a change in the acute freezing response of mice during the training session.

One day later, the mice were exposed to four CS stimuli in a different context to test for the retrieval of an auditory-cued fear memory. Mice showed moderate levels of contextual freezing before the first CS, and presentation of the CSs led to robust increases in freezing in both groups (Figure 5G). Quantification showed that the freezing levels during the CS presentations were unchanged between the groups (Figure 5H [left]: $p = 0.497$, $F_{1,19} = 0.481$; two-way RM ANOVA). On the other hand, inspection of the time-resolved freezing traces suggests that mice in the halorhodopsin group showed a slowed return from high freezing after the cessation of each CS (see Figure 5G; red traces). To quantify this effect, we analyzed the freezing levels during late post-CS windows of 30-s length (Figure 5G, lower gray bars). Despite a trend in the data indicating higher freezing levels late after each CS, there was no statistically significant difference in the freezing levels (Figure 5H [right]: $p = 0.0581$, $F_{1,19} = 4.068$, two-way RM ANOVA; Figure 5I [right]: $p = 0.0581$, $t_{19} = 2.017$, t test). Taken together, activity of pInsCx axons in the LA during shock presentations is not necessary for the formation of an auditory-cued fear memory. Nevertheless, silencing of the pInsCx projection caused a trend toward a slowed return of freezing after the end of each CS.

Having found that optogenetic silencing of pInsCx axons in the anterior LA during footshock presentations has no effect on fear learning (Figure 5), we next optogenetically silenced principal neurons in the pInsCx, using archaerhodopsin (Arch; Figure S5). This manipulation did not cause a significant change in the strength of auditory-cued fear memory (Figures S5F–S5H; $p = 0.654$, two-way RM ANOVA; $N = 11$ and $N = 11$ mice in the Arch and eGFP control groups), in keeping with the results from the more specific silencing of pInsCx axons in the LA (Figure 5). Furthermore, there was no significant change in late CS-driven freezing during the recall session ($p = 0.659$, two-way RM ANOVA). Control experiments with *in vivo* single-unit recordings showed that the activation of Arch led to a significant reduction of US-driven AP-firing in pInsCx principal neurons; nevertheless, a certain residual activity remained (Figures S5P–S5S). These experiments provide evidence against the idea that footshock-driven activity of pInsCx principal neurons is necessary for the formation of an auditory-cued fear memory. Taken together,

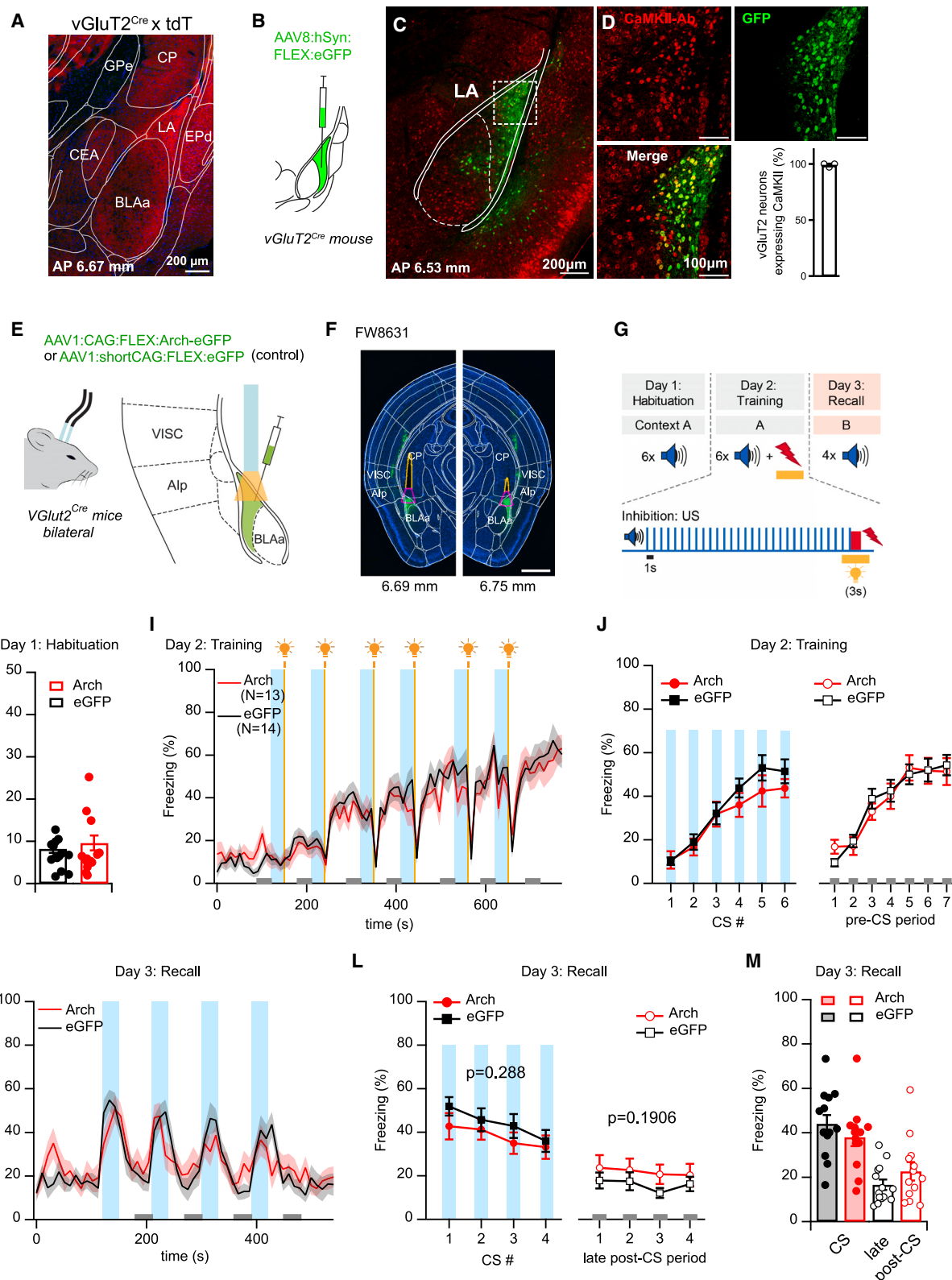
neither silencing of pInsCx axons in the LA (Figure 5) nor direct silencing of pInsCx principal neurons (Figure S5) reveals a role for US-driven activity of pInsCx principal neurons in fear learning.

US signaling in principal neurons of the anterior LA has a limited role in fear learning

It has been shown recently that optogenetic silencing of US-driven activity in indirect pathway neurons of the ventral tail striatum (vTS) leads to a slowed return of CS-induced freezing during fear memory recall.⁴⁶ Because the anterior LA and the vTS are adjacent, and both receive strong glutamatergic projections from the pInsCx (Figure 1B and Kintscher et al.⁴⁶), it is possible that the trend toward a slowed return from CS-induced freezing in the experiments of Figure 5 was caused by an off-target effect in the vTS. To investigate this possibility, we next studied the role of US-induced AP firing of principal neurons of the anterior LA for fear learning.

For this experiment, we used Arch-mediated silencing of neuronal somata in the anterior LA. We employed VGlut2^{Cre} mice because we found that this line drives Cre expression in the anterior LA but not in principal neurons of the neighboring vTS (Figures 6A–6D). First, in VGlut2^{Cre} × tdT mice, there was only a weak tdTomato expression in the vTS, probably caused by incoming glutamatergic axons (Figure 6A; vTS is labeled as “CP”). Second, infusion of an adeno-associated virus (AAV) vector driving the Cre-dependent expression of eGFP revealed that virtually every transduced neuron in the anterior LA was CaMKII positive as revealed by immunohistochemistry (Figures 6B–6D). Thus, using VGlut2^{Cre} mice allows us to drive Cre-dependent Arch expression selectively in principal neurons of the anterior LA while sparing the medially adjacent vTS.

For the optogenetic *in vivo* experiment, a Cre-dependent AAV vector driving the expression of Arch was injected bilaterally into the anterior LA, and optic fibers were implanted above the injection sites (Figures 6E and 6F). Because the anterior LA is a small brain area, we had to exclude mice in which the optic fibers or the expression of Arch were not well targeted ($N = 9$ mice out of $N = 22$ Arch mice were excluded; Figure S7). During the training session, we applied green laser light pulses centered on the footshock presentations to silence US-driven AP activity (Figure 6G). This did not cause a difference in the freezing behavior during the training day (Figures 6I and 6J; $p = 0.331$ and 0.905 for the CS and pre-CS periods; $N = 13$ and $N = 14$ Arch- and eGFP-expressing mice, respectively; two-way RM ANOVA). During the fear memory recall session, presentation of the CS in a novel context caused robust freezing in both the Arch group and the eGFP group (Figure 6K). Quantitative analysis showed that the amount of freezing during the CS and during the late post-CS times were not different (Figure 6L, left and right; $p = 0.288$ and 0.191 ; $N = 13$ and $N = 14$ Arch- and eGFP mice, respectively; two-way RM ANOVA). Furthermore, grouping the data from the $n = 4$ CS presentations did not reveal significant differences either for freezing during the CS or for freezing at late times after the CS ($p = 0.288$ and 0.191 ; Figure 6M, left and right, respectively; t test). We therefore conclude that the trend toward a slowed freezing decay that we observed upon silencing of the pInsCx axons in the LA (Figures 5G and 5H) is likely an off-target effect, because it was not observed after direct silencing of principal



(legend on next page)

neurons in the anterior LA. Furthermore, US-driven activity of principal neurons in the anterior LA is not necessary for the formation of an auditory-cued fear memory (see [discussion](#)).

DISCUSSION

The posterior insular cortex (plnsCx) codes for somatosensory, nociceptive, and temperature information,^{37,38,65} and imaging studies in humans have shown that this cortical area is part of a larger network that processes pain-related information.^{35,36,66} Here, we have defined a glutamatergic projection from the plnsCx to the anterior LA in mice and have studied the transmission of US information at this pathway and its relation to fear learning. Using anatomical tracing and optogenetically assisted circuit mapping, we found a robust glutamatergic connection from the plnsCx to specific subareas of the BLA complex, including the anterior LA. *In vivo* Ca²⁺ imaging revealed that separate subpopulations of principal neurons in both the plnsCx and the anterior LA code for the onset and the offset of aversive footshocks, employed as the US in fear-learning experiments. Combining Ca²⁺ imaging with optogenetic axon silencing showed that the US-offset response, but not the US-onset response, is transmitted at the plnsCx to anterior LA synapse. *In vivo* pathway-specific optogenetic silencing and silencing of neuronal somata during the footshocks, however, did not show evidence for a role of US-driven activity in the anterior LA for auditory-cued fear learning. The role that US-offset information in the anterior LA might play in aversively motivated behaviors beyond fear learning should be investigated in future studies.

Using antero- and retrograde labeling techniques complemented by optogenetic mapping experiments, we found that the plnsCx makes a robust glutamatergic projection specifically to the anterior LA ([Figures 1](#) and [2](#)). This finding agrees with a recent study showing that an area of the mouse plnsCx coding for skin temperature projects to the LA.³⁹ On the other hand, a study employing anatomical output tracing for three mouse in-

sula areas found weak axonal labeling in the LA, whereas axons in the CeA were clearly observed.⁴² It is possible that differences in the targeting of anterograde vectors are responsible for the apparent differences between our and the previous study. In addition, since the plnsCx selectively projects to the anterior LA, averaging the fluorescence of output axons over the entire brain areas⁴² might have led to an under-representation of projections targeting subregions of the LA. In summary, the plnsCx makes a robust glutamatergic projection to the anterior LA, confirming and extending recent anatomical data.^{39,67} Together, these studies suggest that the plnsCx-to-LA connection is conserved between mice (this study; Bokiniec et al.^{39,67}; Krabbe et al.^{39,67}), rats⁴⁷ and primates.^{9,48}

To investigate how information about aversive footshocks is processed in the plnsCx and the anterior LA, we performed *in vivo* Ca²⁺ imaging during fear learning in both brain areas. We found, not unexpectedly,³⁷ that a subpopulation of plnsCx principal neurons responded to the onset of the footshocks ([Figure 3](#)). Furthermore, we discovered that a separate, smaller subpopulation of plnsCx principal neurons responded at the end of aversive foot-shock stimulation; we call these “US-offset” responses. Previous work found responses to the offset of aversive stimulation in dopamine midbrain neurons, and such responses have been implicated in pain relief.⁶⁸ Recently, specific ventral tegmental area (VTA) dopamine neurons projecting to the nucleus accumbens (ACB) were studied in fear and extinction learning.⁶⁹ These neurons display responses after the CS during early phases of extinction, when the subject predicts that the CS is followed by a negative outcome (“US-omission” responses). Furthermore, the VTA neurons showed biphasic responses to footshocks, including a late slow component⁶⁹ reminiscent of the US-offset response that we found here. The plnsCx makes a projection to the ACB ([Figure 1](#); Gehrlach et al.²⁶, Wang et al.²⁸); it will therefore be interesting to investigate whether there is a relation of the US-offset responses in the plnsCx with possible US-offset responses in the ACB. Thus, US-offset responses have been previously

Figure 6. Footshock-driven activity of principal neurons in the anterior LA has a limited role in fear learning

- (A) td-Tomato fluorescence image on the level of the anterior LA taken from a VGluT2^{Cre} × tdT mouse.
 - (B) Experimental approach employing infusion of AAV8:hSyn:FLEX-eGFP into the anterior LA of a VGluT2^{Cre} mouse.
 - (C and D) Images of eGFP fluorescence (green) and anti-CamKII immunofluorescence (red) in the anterior LA and adjacent brain areas of a VGluT2^{Cre} mouse. Insets in (D) show the region indicated by the box in (C). Quantification showed that 99.0% ± 1.2% of VGluT2^{Cre+} neurons expressed CamKII (D, lower right; n = 241 eGFP⁺ neurons analyzed from n = 2 sections from N = 1 mouse).
 - (E) Scheme for the *in vivo* optogenetic experiment with bilateral expression of Arch-eGFP (or eGFP in control mice) in the anterior LA.
 - (F) Post hoc histological validation of bilateral Arch-eGFP expression in the anterior LA and optical fiber positioning in an example mouse (see also [Figure S7](#) for the histological images for all Arch mice).
 - (G) Scheme of the timing of optogenetic inhibition of anterior LA neurons, centered on the footshock presentations during the training session.
 - (H) Average and individual data points for freezing during the CS periods during the habituation session for mice in the Arch and eGFP groups (N = 13 and N = 14; red and black data points, respectively).
 - (I) Time-resolved average freezing behavior for mice in the Arch and control groups during the training session (red, and black traces, N = 13 and N = 14, respectively). Vertical blue bars indicate the CS; yellow bars indicate the time of footshock presentations.
 - (J) Quantification of freezing during the 30-s CS and pre-CS epochs (left and right panel, respectively). Freezing during neither the CS nor the no-CS periods was significantly different between the groups (see [results](#) for statistical parameters).
 - (K) Time-resolved average freezing of mice in the Arch and control group during fear memory recall (N = 13 and N = 14 mice, respectively).
 - (L) Quantification of freezing during the CS periods (left) and during the 30-s late post-CS periods (right) during fear memory recall. See [results](#) for parameter values of statistical tests.
 - (M) Average and individual data for freezing during the CS (filled dots and bars) and late post-CS periods (open dots and bars), averaged across the four CS presentations.
- Scale bars, 200 μm (A and C), 100 μm (D), and 1 mm (F). In (H), (J), (L), and (M), data are mean ± SEM. In (I) and (K), traces and light-color hues indicate mean ± SEM. See also [Figures S5](#) and [S7](#).

observed in midbrain dopamine neurons,^{68,69} to which our observations in the plnsCx add. How US-offset responses are computed, and which role they play in aversively motivated behaviors or else in the return from such behavior, needs to be addressed in future studies.

We initially hypothesized that the posterior insula, known to code for nociceptive and somatosensory information,³⁷ transmits information about aversive footshocks to the LA, where this depolarizing signal could contribute to a teaching signal instructing associative synaptic plasticity during fear learning (see also Herry and Johansen^{19–21} and Palchaudhuri et al.^{19–21} for the concept of teaching signal). Nevertheless, the experimental evidence that we obtained does not support this model. First, the plnsCx codes for both US-onset and US-offset information, but only the US-offset information is transmitted to the anterior LA. Second, anatomy and optogenetic mapping show that the plnsCx specifically connects to the anterior LA, whereas information from the auditory cortex reaches the LA in more posterior regions (Figure 1). Moreover, *in vivo* optogenetic silencing experiments did not reveal a behavioral role for US-driven activity either at the plnsCx-to-anterior-LA connection or in principal neurons of the anterior LA (Figures 5 and 6). Thus, contrary to our initial hypothesis, the plnsCx does not transmit US information to the LA that is relevant for the formation of an auditory-cued fear memory.

The LA has been shown in rats^{3,13,14} and mice^{70,71} to be crucial for fear learning. However, targeting the anterior LA, we have been unable to demonstrate a role for US-driven activity in this brain area for fear learning. The explanation for this apparent discrepancy might lie in the intricate specificity with which synaptic input streams target the LA along its anterior-posterior (a-p) axis (Figure 1). Thus, it has been shown that long-term potentiation at inputs from the ventral auditory cortex¹⁵ and the auditory thalamus¹³ contributes to fear memory expression. On the other hand, the anterior LA, which we have silenced here (Figures 6 and S7), does not receive a high density of auditory inputs. Thus, we assume that the posterior LA, which receives auditory inputs at a higher density (Figure 1), is more critically involved in laying down an auditory-cued fear memory engram, a possibility that we are currently investigating (J.W., O.K., and R.S., unpublished data).

Our finding that US-onset signals in the anterior LA persist after the silencing of plnsCx afferents (Figure 4) indicates that other afferent systems must carry information about aversive footshocks to the LA. These inputs might include excitatory projections from non-lemniscal auditory thalamic areas^{7,25} and from the ventral auditory cortex (Dalmay et al.^{8–10} and see Figure 1). These areas, which in earlier work have been implied to selectively convey auditory information to the LA,² have more recently been shown to process footshock information as well^{7,10,25,72} (see Palchaudhuri et al.^{19–21} for a review). In addition, US information might be conveyed to the LA by further, so-far understudied brain areas. These might include midline thalamic areas,⁷³ which were recently shown to receive nociceptive input from the parabrachial nucleus,⁷⁴ the paraventricular thalamus,⁷⁵ and possibly spinal inputs conveying pain-related information to the forebrain.⁷⁶

When we optogenetically silenced the inputs from the plnsCx in the anterior LA, we observed a trend toward a slowed return

from freezing upon CS termination (Figures 5G and 5H). This effect likely represented an off-target effect because it was not observed after optogenetic silencing of principal neuron somata in the anterior LA (Figure 6). This off-target action was probably caused by unwanted silencing of axons projecting from the plnsCx to the vTS (see Figure 1B for the anatomy). Indeed, we recently found that optogenetic silencing of US-driven activity of indirect pathway neurons in the vTS produces a similar behavioral effect, which suggested that vTS indirect pathway neurons contribute to a swift return from freezing upon CS termination.⁴⁶ Thus, the halorhodopsin-mediated axon silencing employed here, besides inactivating plnsCx axons in the LA as revealed by Ca²⁺ imaging (Figure 4), has likely also caused a decreased activity of plnsCx axons in the neighboring vTS.

The plnsCx projects to several other brain areas beyond the anterior LA (Figure 1). Thus, US-onset signals could be transmitted from the plnsCx to other brain areas, where they might be involved in driving plasticity related to fear learning. Optogenetic silencing, however, did not reveal a role for US-driven activity of plnsCx principal neurons in fear learning (Figure S5; but see also “[limitations of the study](#)”). Recent work has shown roles for CeA projectors in the posterior insula³⁰ as well as in more anterior regions of the insula²⁸ in fear learning. Thus, it remains possible that in our optogenetic silencing experiments in the plnsCx, CeA projectors were not efficiently covered. Another recent study found a selective role of neurons in the anterior insula in coding for anxiety states and attributed this role to a projection to the basal amygdala (BA), another output projection of the insula to the amygdala (Nicolas et al.^{26–33}, see also Figure 1C). The transmission of sensory information, or behavioral state information at the projections from the insula to the CeA and BA, could be investigated in more detail in future work.

In summary, we have defined a glutamatergic projection from the posterior insular cortex, which provides the anterior LA with information about the end of aversive shock events. On the other hand, the plnsCx does not transmit fast-onset information about aversive footshocks to the LA, and footshock-driven activity in the anterior LA is not necessary for fear learning. Furthermore, auditory afferents target the posterior LA and, thus, different functions of the anterior vs. posterior LA in fear learning seem likely. Given that the activity of both the insular cortex and the amygdala are altered in various forms of psychiatric disease,^{77–79} it is highly relevant to further investigate the circuit organization of insula-amygdala networks. This will improve our understanding of how these networks survey both extero- and interoceptive signals from the body,^{27,37} thereby helping to guide adaptive behavior and learning in response to threats.

Limitations of the study

We cannot exclude the possibility that methodological limitations in the optogenetic silencing methods may have masked small behavioral effects. Thus, we showed in control experiments that optogenetic silencing of Arch-expressing neurons led to a significant reduction of US-driven AP firing in the plnsCx, but some residual activity remained (Figures S5P–S5S). Also, limitations in the neuronal tropism of AAV vectors^{80,81} could

lead to the sparing of Arch expression in a subpopulation of principal neurons that might be important for fear learning. Finally, because of the intricate neighborhood of output structures of the pInsCx, it has proven difficult to selectively inhibit projections of the pInsCx to the anterior LA without affecting collaterals to other brain areas.

RESOURCE AVAILABILITY

Lead contact

Please direct all requests to the lead contact, Dr. Ralf Schneggenburger (ralf.schneggenburger@epfl.ch).

Materials availability

The custom viral vector AAV8:hSyn:FLEX:synaptophysin-mCherry:IRES:eGFP can be purchased from the Bertarelli Foundation Gene Therapy Platform at EPFL, Geneva, Switzerland (ptbtg@groupe.epfl.ch).

Data and code availability

- The data generated during this study is publicly available at the Zenodo repository (<https://doi.org/10.5281/zenodo.14604021>).
- Original code has been deposited at GitHub repository and is publicly available. The links are given in the [key resources table](#).
- Any additional information required to reanalyze the data reported in this paper is available from the [lead contact](#) upon request.

ACKNOWLEDGMENTS

We thank Heather Murray and Melanie Sipion for support with mouse genotyping and histology, Dr. Michael Kintscher for input regarding mouse behavior analysis, Dr. Carmen Sandi for sharing equipment, Dr. Bernard Schneider and the EPFL Bertarelli Foundation Gene Therapy Platform for AAV vector packaging, Dr. Nicolas Chiaruttini and Dr. Olivier Burri for help with the ABBA-QuPath analysis pipeline, and Dr. Linda Mhalla (EPFL, School of Basic Sciences) for advice on statistical testing. Images were acquired at the bio-optical imaging platform of EPFL (BiOP). The study was supported by grants from the Swiss National Science Foundation (SNF) 31003A_176332/1 and 310030_204587/1 and from the NCCR Synapsy – The synaptic bases of mental disease, project P28.

AUTHOR CONTRIBUTIONS

S.P., D.O., O.K., and R.S. conceptualized the study. S.P. performed behavior experiments, anatomy, slice electrophysiology, *in vivo* Ca²⁺ imaging, and data analysis. D.O. performed *in vivo* electrophysiology, behavior experiments, and data analysis. B.-X.L. performed *in vivo* Ca²⁺ imaging and data analysis. J.W. and O.K. performed behavior experiments, anatomy, and data analysis. O.K. and D.O. wrote custom scripts for analysis. R.S. and S.P. wrote the manuscript, which was edited by all authors. R.S. and O.K. were involved in supervision.

DECLARATION OF INTERESTS

The authors declare no competing interests.

STAR METHODS

Detailed methods are provided in the online version of this paper and include the following:

- KEY RESOURCES TABLE
- EXPERIMENTAL MODEL AND STUDY PARTICIPANTS DETAILS
- METHOD DETAILS
 - Plasmid DNA cloning
 - Viral vectors
 - Stereotaxic coordinates

- Stereotaxic surgery
 - Fear learning protocol
 - In-vivo electrophysiology
 - Miniature - Microscope Ca²⁺-imaging
 - Slice electrophysiology
 - Histology and immunohistochemistry
- QUANTIFICATION AND STATISTICAL ANALYSIS
 - Behavior data analysis
 - Data analysis for *in-vivo* unit activity
 - Data analysis for slice electrophysiology
 - Ca²⁺-imaging data analysis
 - Histological image analysis
 - Statistical analysis

SUPPLEMENTAL INFORMATION

Supplemental information can be found online at <https://doi.org/10.1016/j.celrep.2025.115320>.

Received: April 21, 2023

Revised: March 21, 2024

Accepted: January 27, 2025

Published: February 15, 2025

REFERENCES

1. Janak, P.H., and Tye, K.M. (2015). From circuits to behaviour in the amygdala. *Nature* 517, 284–292. <https://doi.org/10.1038/nature14188>.
2. LeDoux, J.E. (2000). Emotion circuits in the brain. *Annu. Rev. Neurosci.* 23, 155–184. <https://doi.org/10.1146/annurev.neuro.23.1.155>.
3. LeDoux, J.E., Cicchetti, P., Xagoraris, A., and Romanski, L.M. (1990). The lateral amygdaloid nucleus: sensory interface of the amygdala in fear conditioning. *J. Neurosci.* 10, 1062–1069.
4. Quirk, G.J., Repa, C., and LeDoux, J.E. (1995). Fear conditioning enhances short-latency auditory responses of lateral amygdala neurons: parallel recordings in the freely behaving rat. *Neuron* 15, 1029–1039.
5. Grewe, B.F., Gründemann, J., Kitch, L.J., Lecoq, J.A., Parker, J.G., Marshall, J.D., Larkin, M.C., Jercog, P.E., Grenier, F., Li, J.Z., et al. (2017). Neural ensemble dynamics underlying a long-term associative memory. *Nature* 543, 670–675. <https://doi.org/10.1038/nature21682>.
6. LeDoux, J.E., Farb, C., and Ruggiero, D.A. (1990). Topographic organization of neurons in the acoustic thalamus that project to the amygdala. *J. Neurosci.* 10, 1043–1054.
7. Barsy, B., Kocsis, K., Magyar, A., Babiczky, Á., Szabó, M., Veres, J.M., Hillier, D., Ulbert, I., Yizhar, O., and Mátýás, F. (2020). Associative and plastic thalamic signaling to the lateral amygdala controls fear behavior. *Nat. Neurosci.* 23, 625–637. <https://doi.org/10.1038/s41593-020-0620-z>.
8. Romanski, L.M., and LeDoux, J.E. (1993). Information cascade from primary auditory cortex to the amygdala: corticocortical and corticoamygdaloid projections of temporal cortex in the rat. *Cerebr. Cortex* 3, 515–532.
9. McDonald, A.J. (1998). Cortical pathways to the mammalian amygdala. *Prog. Neurobiol.* 55, 257–332.
10. Dalmary, T., Abs, E., Poorthuis, R.B., Hartung, J., Pu, D.L., Onasch, S., Lozano, Y.R., Signoret-Genest, J., Tovote, P., Gjorgjeva, J., and Letzkus, J.J. (2019). A critical role for neocortical processing of threat memory. *Neuron* 104, 1180–1194.e7. <https://doi.org/10.1016/j.neuron.2019.09.025>.
11. Rogan, M.T., and LeDoux, J.E. (1995). LTP is accompanied by commensurate enhancement of auditory-evoked responses in a fear conditioning circuit. *Neuron* 15, 127–136.
12. McKernan, M.G., and Shinnick-Gallagher, P. (1997). Fear conditioning induces a lasting potentiation of synaptic currents in vitro. *Nature* 390, 607–611. <https://doi.org/10.1038/37605>.

13. Rumpel, S., LeDoux, J., Zador, A., and Malinow, R. (2005). Postsynaptic receptor trafficking underlying a form of associative learning. *Science* **308**, 83–88. <https://doi.org/10.1126/science.1103944>.
14. Nabavi, S., Fox, R., Proulx, C.D., Lin, J.Y., Tsien, R.Y., and Malinow, R. (2014). Engineering a memory with LTD and LTP. *Nature* **511**, 348–352. <https://doi.org/10.1038/nature13294>.
15. Kim, W.B., and Cho, J.H. (2017). Encoding of discriminative fear memory by input-specific LTP in the amygdala. *Neuron* **95**, 1129–1146.e5. <https://doi.org/10.1016/j.neuron.2017.08.004>.
16. Johansen, J.P., Hamanaka, H., Monfils, M.H., Behnia, R., Deisseroth, K., Blair, H.T., and LeDoux, J.E. (2010). Optical activation of lateral amygdala pyramidal cells instructs associative fear learning. *Proc. Natl. Acad. Sci. USA* **107**, 12692–12697. <https://doi.org/10.1073/pnas.1002418107>.
17. Gore, F., Schwartz, E.C., Brangers, B.C., Aladi, S., Stujenske, J.M., Likhithik, E., Russo, M.J., Gordon, J.A., Salzman, C.D., and Axel, R. (2015). Neural representations of unconditioned stimuli in basolateral amygdala mediate innate and learned responses. *Cell* **162**, 134–145. <https://doi.org/10.1016/j.cell.2015.06.027>.
18. Zhang, X., and Li, B. (2018). Population coding of valence in the basolateral amygdala. *Nat. Commun.* **9**, 5195. <https://doi.org/10.1038/s41467-018-07679-9>.
19. Sigurdsson, T., Doyère, V., Cain, C.K., and LeDoux, J.E. (2007). Long-term potentiation in the amygdala: a cellular mechanism of fear learning and memory. *Neuropharmacology* **52**, 215–227. <https://doi.org/10.1016/j.neuropharm.2006.06.022>.
20. Herry, C., and Johansen, J.P. (2014). Encoding of fear learning and memory in distributed neuronal circuits. *Nat. Neurosci.* **17**, 1644–1654. <https://doi.org/10.1038/nn.3869>.
21. Palchaudhuri, S., Osypenko, D., and Schneggenburger, R. (2024). Fear learning: An evolving picture for plasticity at synaptic afferents to the amygdala. *Neuroscientist* **30**, 87–104. <https://doi.org/10.1177/10738584221108083>.
22. Johansen, J.P., Diaz-Mataix, L., Hamanaka, H., Ozawa, T., Ycu, E., Koivumaa, J., Kumar, A., Hou, M., Deisseroth, K., Boyden, E.S., and LeDoux, J.E. (2014). Hebbian and neuromodulatory mechanisms interact to trigger associative memory formation. *Proc. Natl. Acad. Sci. USA* **111**, E5584–E5592. <https://doi.org/10.1073/pnas.1421304111>.
23. Jiang, L., Kundu, S., Lederman, J.D., López-Hernández, G.Y., Ballinger, E.C., Wang, S., Talmage, D.A., and Role, L.W. (2016). Cholinergic signaling controls conditioned fear behaviors and enhances plasticity of cortical-amygdala circuits. *Neuron* **90**, 1057–1070. <https://doi.org/10.1016/j.neuron.2016.04.028>.
24. Tang, W., Kochubey, O., Kintscher, M., and Schneggenburger, R. (2020). A VTA to basal amygdala dopamine projection contributes to signal salient somatosensory events during fear learning. *J. Neurosci.* **40**, 3969–3980. <https://doi.org/10.1523/JNEUROSCI.1796-19.2020>.
25. Taylor, J.A., Hasegawa, M., Benoit, C.M., Freire, J.A., Theodore, M., Ganea, D.A., Innocenti, S.M., Lu, T., and Gründemann, J. (2021). Single cell plasticity and population coding stability in auditory thalamus upon associative learning. *Nat. Commun.* **12**, 2438. <https://doi.org/10.1038/s41467-021-22421-8>.
26. Gehrlach, D.A., Dolensek, N., Klein, A.S., Roy Chowdhury, R., Matthys, A., Junghänel, M., Gaitanos, T.N., Podgornik, A., Black, T.D., Reddy Vaka, N., et al. (2019). Aversive state processing in the posterior insular cortex. *Nat. Neurosci.* **22**, 1424–1437. <https://doi.org/10.1038/s41593-019-0469-1>.
27. Klein, A.S., Dolensek, N., Weiand, C., and Gogolla, N. (2021). Fear balance is maintained by bodily feedback to the insular cortex in mice. *Science* **374**, 1010–1015. <https://doi.org/10.1126/science.abj8817>.
28. Wang, Q., Zhu, J.J., Wang, L., Kan, Y.P., Liu, Y.M., Wu, Y.J., Gu, X., Yi, X., Lin, Z.J., Wang, Q., et al. (2022). Insular cortical circuits as an executive gateway to decipher threat or extinction memory via distinct subcortical pathways. *Nat. Commun.* **13**, 5540. <https://doi.org/10.1038/s41467-022-33241-9>.
29. Nicolas, C., Ju, A., Wu, Y., Eldirdiri, H., Delcasso, S., Couderc, Y., Fornari, C., Mitra, A., Supiot, L., Vérité, A., et al. (2023). Linking emotional valence and anxiety in a mouse insula–amygdala circuit. *Nat. Commun.* **14**, 5073. <https://doi.org/10.1038/s41467-023-40517-1>.
30. Kargl, D., Kaczanowska, J., Ułomska, S., Groessl, F., Piszczełek, L., Lazovic, J., Buehler, K., and Haubensak, W. (2020). The amygdala instructs insular feedback for affective learning. *Elife* **9**, e60336. <https://doi.org/10.7554/elife.60336>.
31. Wang, L., Gillis-Smith, S., Peng, Y., Zhang, J., Chen, X., Salzman, C.D., Ryba, N.J.P., and Zuker, C.S. (2018). The coding of valence and identity in the mammalian taste system. *Nature* **558**, 127–131. <https://doi.org/10.1038/s41586-018-0165-4>.
32. Schiff, H.C., Bouhuys, A.L., Yu, K., Penzo, M.A., Li, H., He, M., and Li, B. (2018). An insula-central amygdala circuit for guiding tastant-reinforced choice behavior. *J. Neurosci.* **38**, 1418–1429. <https://doi.org/10.1523/JNEUROSCI.1773-17.2017>.
33. Kusumoto-Yoshida, I., Liu, H., Chen, B.T., Fontanini, A., and Bonci, A. (2015). Central role for the insular cortex in mediating conditioned responses to anticipatory cues. *Proc. Natl. Acad. Sci. USA* **112**, 1190–1195. <https://doi.org/10.1073/pnas.1416573112>.
34. Gogolla, N. (2017). The insular cortex. *Curr. Biol.* **27**, R580–R586. <https://doi.org/10.1016/j.cub.2017.05.010>.
35. Apkarian, A.V., Bushnell, M.C., Treede, R.D., and Zubieta, J.K. (2005). Human brain mechanisms of pain perception and regulation in health and disease. *Eur. J. Pain* **9**, 463–484. <https://doi.org/10.1016/j.ejpain.2004.11.001>.
36. Coghill, R.C. (2020). The distributed nociceptive system: A framework for understanding pain. *Trends Neurosci.* **43**, 780–794. <https://doi.org/10.1016/j.tins.2020.07.004>.
37. Rodgers, K.M., Benison, A.M., Klein, A., and Barth, D.S. (2008). Auditory, somatosensory, and multisensory insular cortex in the rat. *Cerebr. Cortex* **18**, 2941–2951. <https://doi.org/10.1093/cercor/bhn054>.
38. Vestergaard, M., Carta, M., Guney, G., and Poulet, J.F.A. (2023). The cellular coding of temperature in the mammalian cortex. *Nature* **614**, 725–731. <https://doi.org/10.1038/s41586-023-05705-5>.
39. Bokinić, P., Whitmire, C.J., Leva, T.M., and Poulet, J.F.A. (2023). Brain-wide connectivity map of mouse thermosensory cortices. *Cerebr. Cortex* **33**, 4870–4885. <https://doi.org/10.1093/cercor/bhac386>.
40. Cechetto, D.F., and Saper, C.B. (1987). Evidence for a viscerotopic sensory representation in the cortex and thalamus in the rat. *J. Comp. Neurol.* **262**, 27–45. <https://doi.org/10.1002/cne.902620104>.
41. Ponserre, M., Peters, C., Fermani, F., Conzelmann, K.K., and Klein, R. (2020). The insula cortex contacts distinct output streams of the central amygdala. *J. Neurosci.* **40**, 8870–8882. <https://doi.org/10.1523/JNEUROSCI.0567-20.2020>.
42. Gehrlach, D.A., Weiand, C., Gaitanos, T.N., Cho, E., Klein, A.S., Hennrich, A.A., Conzelmann, K.K., and Gogolla, N. (2020). A whole-brain connectivity map of mouse insular cortex. *Elife* **9**, e55585. <https://doi.org/10.7554/elife.55585>.
43. Zhang-Molina, C., Schmit, M.B., and Cai, H. (2020). Neural Circuit Mechanism Underlying the Feeding Controlled by Insula-Central Amygdala Pathway. *iScience* **23**, 101033. <https://doi.org/10.1016/j.isci.2020.101033>.
44. Takemoto, M., Kato, S., Kobayashi, K., and Song, W.J. (2023). Dissection of insular cortex layer 5 reveals two sublayers with opposing modulatory roles in appetitive drinking behavior. *iScience* **26**, 106985. <https://doi.org/10.1016/j.isci.2023.106985>.
45. Hunnicutt, B.J., Jongbloets, B.C., Birdsong, W.T., Gertz, K.J., Zhong, H., and Mao, T. (2016). A comprehensive excitatory input map of the striatum reveals novel functional organization. *Elife* **5**, e19103. <https://doi.org/10.7554/elife.19103>.

46. Kintscher, M., Kochubey, O., and Schneggenburger, R. (2023). A striatal circuit balances learned fear in the presence and absence of sensory cues. *eLife* 12, e75703. <https://doi.org/10.7554/eLife.75703>.
47. Shi, C.J., and Cassell, M.D. (1998). Cascade projections from somatosensory cortex to the rat basolateral amygdala via the parietal insular cortex. *J. Comp. Neurol.* 399, 469–491.
48. Mufson, E.J., Mesulam, M.M., and Pandya, D.N. (1981). Insular interconnections with the amygdala in the rhesus monkey. *Neuroscience* 6, 1231–1248.
49. Allen Institute for Brain Science (2014). Allen Mouse Brain Atlas. <http://mouse.brain-map.org/>.
50. Madisen, L., Zwingman, T.A., Sunkin, S.M., Oh, S.W., Zariwala, H.A., Gu, H., Ng, L.L., Palmiter, R.D., Hawrylycz, M.J., Jones, A.R., et al. (2010). A robust and high-throughput Cre reporting and characterization system for the whole mouse brain. *Nat. Neurosci.* 13, 133–140. [https://doi.org/10.1038/nn.2467.nn.2467.\[pii\]](https://doi.org/10.1038/nn.2467.nn.2467.[pii]).
51. Sürmeli, G., Marcu, D.C., McClure, C., Garden, D.L.F., Pastoll, H., and Nolan, M.F. (2015). Molecularly defined circuitry reveals input-output segregation in deep layers of the medial entorhinal cortex. *Neuron* 88, 1040–1053. <https://doi.org/10.1016/j.neuron.2015.10.041>.
52. Yasui, Y., Breder, C.D., Saper, C.B., and Cechedo, D.F. (1991). Autonomic responses and efferent pathways from the insular cortex in the rat. *J. Comp. Neurol.* 303, 355–374. <https://doi.org/10.1002/cne.903030303>.
53. Kimura, A., Imbe, H., and Donishi, T. (2010). Efferent connections of an auditory area in the caudal insular cortex of the rat: anatomical nodes for cortical streams of auditory processing and cross-modal sensory interactions. *Neuroscience* 166, 1140–1157. <https://doi.org/10.1016/j.neuroscience.2010.01.032>.
54. Gauriau, C., and Bernard, J.F. (2004). Posterior triangular thalamic neurons convey nociceptive messages to the secondary somatosensory and insular cortices in the rat. *J. Neurosci.* 24, 752–761. <https://doi.org/10.1523/Jneurosci.3272-03.2004>.
55. Chen, X., Gabitto, M., Peng, Y., Ryba, N.J.P., and Zuker, C.S. (2011). A gustotopic map of taste qualities in the mammalian brain. *Science* 333, 1262–1266. <https://doi.org/10.1126/science.1204076>.
56. Samuelson, C.L., Gardner, M.P.H., and Fontanini, A. (2013). Thalamic contribution to cortical processing of taste and expectation. *J. Neurosci.* 33, 1815–1827. <https://doi.org/10.1523/JNEUROSCI.4026-12.2013>.
57. Gauriau, C., and Bernard, J.F. (2004). A comparative reappraisal of projections from the superficial laminae of the dorsal horn in the rat: The forebrain. *J. Comp. Neurol.* 468, 24–56. <https://doi.org/10.1002/cne.10873>.
58. Frangeul, L., Porrero, C., Garcia-Amado, M., Maimone, B., Maniglier, M., Clascá, F., and Jabaoudon, D. (2014). Specific activation of the paralemniscal pathway during nociception. *Eur. J. Neurosci.* 39, 1455–1464. <https://doi.org/10.1111/ejn.12524>.
59. Petreanu, L., Huber, D., Sobczyk, A., and Svoboda, K. (2007). Channelrhodopsin-2-assisted circuit mapping of long-range callosal projections. *Nat. Neurosci.* 10, 663–668.
60. Klapoetke, N.C., Murata, Y., Kim, S.S., Pulver, S.R., Birdsey-Benson, A., Cho, Y.K., Morimoto, T.K., Chuong, A.S., Carpenter, E.J., Tian, Z., et al. (2014). Independent optical excitation of distinct neural populations. *Nat. Methods* 11, 338–346. <https://doi.org/10.1038/nmeth.2836>.
61. Litvina, E.Y., and Chen, C. (2017). Functional Convergence at the Retino-geniculate Synapse. *Neuron* 96, 330–338.e5. <https://doi.org/10.1016/j.neuron.2017.09.037>.
62. Gjoni, E., Zenke, F., Bouhours, B., and Schneggenburger, R. (2018). Specific synaptic input strengths determine the computational properties of excitation-inhibition integration in a sound localization circuit. *J. Physiol.* 596, 4945–4967. <https://doi.org/10.1113/JP276012>.
63. Ghosh, K.K., Burns, L.D., Cocker, E.D., Nimmerjahn, A., Ziv, Y., Gamal, A.E., and Schnitzer, M.J. (2011). Miniaturized integration of a fluorescence microscope. *Nat. Methods* 8, 871–878. <https://doi.org/10.1038/nmeth.1694>.
64. Stamatakis, A.M., Schachter, M.J., Gulati, S., Zitelli, K.T., Malanowski, S., Tajik, A., Fritz, C., Trulson, M., and Otte, S.L. (2018). Simultaneous optogenetics and cellular resolution calcium imaging during active behavior using a miniaturized microscope. *Front. Neurosci.* 12, 496. <https://doi.org/10.3389/fnins.2018.00496>.
65. Benison, A.M., Chumachenko, S., Harrison, J.A., Maier, S.F., Falci, S.P., Watkins, L.R., and Barth, D.S. (2011). Caudal granular insular cortex is sufficient and necessary for the long-term maintenance of allodynic behavior in the rat attributable to mononeuropathy. *J. Neurosci.* 31, 6317–6328. <https://doi.org/10.1523/JNEUROSCI.0076-11.2011>.
66. Kuner, R., and Kuner, T. (2021). Cellular Circuits in the Brain and Their Modulation in Acute and Chronic Pain. *Physiol. Rev.* 101, 213–258. <https://doi.org/10.1152/physrev.00040.2019>.
67. Krabbe, S., Paradiso, E., d'Aquin, S., Bitterman, Y., Courtin, J., Xu, C., Yonehara, K., Markovic, M., Müller, C., Eichlisberger, T., et al. (2019). Adaptive disinhibitory gating by VIP interneurons permits associative learning. *Nat. Neurosci.* 22, 1834–1843. <https://doi.org/10.1038/s41593-019-0508-y>.
68. Navratilova, E., Atcherley, C.W., and Porreca, F. (2015). Brain circuits encoding reward from pain relief. *Trends Neurosci.* 38, 741–750. <https://doi.org/10.1016/j.tins.2015.09.003>.
69. Salinas-Hernández, X.I., Zafiri, D., Sigurdsson, T., and Duvarci, S. (2023). Functional architecture of dopamine neurons driving fear extinction learning. *Neuron* 111, 3854–3870.e3855. <https://doi.org/10.1016/j.neuron.2023.08.025>.
70. Rashid, A.J., Yan, C., Mercaldo, V., Hsiang, H.L.L., Park, S., Cole, C.J., De Cristofaro, A., Yu, J., Ramakrishnan, C., Lee, S.Y., et al. (2016). Competition between engrams influences fear memory formation and recall. *Science* 353, 383–387. <https://doi.org/10.1126/science.aaf0594>.
71. Santoni, G., Astori, S., Leleu, M., Gläuser, L., Zamora, S.A., Schioppa, M., Tarulli, I., Sandi, C., and Gräff, J. (2024). Chromatin plasticity pre-determines neuronal eligibility for memory trace formation. *Science* 385, ead9982. <https://doi.org/10.1126/science.adg9982>.
72. Weinberger, N.M. (2011). The medial geniculate, not the amygdala, as the root of auditory fear conditioning. *Hear. Res.* 274, 61–74. <https://doi.org/10.1016/j.heares.2010.03.093>.
73. Basbaum, A.I., Bautista, D.M., Scherrer, G., and Julius, D. (2009). Cellular and molecular mechanisms of pain. *Cell* 139, 267–284. <https://doi.org/10.1016/j.cell.2009.09.028>.
74. Deng, J., Zhou, H., Lin, J.K., Shen, Z.X., Chen, W.Z., Wang, L.H., Li, Q., Mu, D., Wei, Y.C., Xu, X.H., and Sun, Y.G. (2020). The Parabrachial Nucleus Directly Channels Spinal Nociceptive Signals to the Intralaminar Thalamic Nuclei, but Not the Amygdala. *Neuron* 107, 909–923.e6. <https://doi.org/10.1016/j.neuron.2020.06.017>.
75. Penzo, M.A., Robert, V., Tucciarone, J., De Bundel, D., Wang, M., Van Aelst, L., Darvas, M., Parada, L.F., Palmiter, R.D., He, M., et al. (2015). The paraventricular thalamus controls a central amygdala fear circuit. *Nature* 519, 455–459. <https://doi.org/10.1038/nature13978>.
76. Cliffer, K.D., Burstein, R., and Giesler, G.J., Jr. (1991). Distributions of spinothalamic, spinohypothalamic, and spinotelencephalic fibers revealed by anterograde transport of PHA-L in rats. *J. Neurosci.* 11, 852–868.
77. Di Martino, A., Yan, C.G., Li, Q., Denio, E., Castellanos, F.X., Alaerts, K., Anderson, J.S., Assaf, M., Bookheimer, S.Y., Dapretto, M., et al. (2014). The autism brain imaging data exchange: towards a large-scale evaluation of the intrinsic brain architecture in autism. *Mol. Psychiatr.* 19, 659–667. <https://doi.org/10.1038/mp.2013.78>.
78. Uddin, L.Q. (2015). Salience processing and insular cortical function and dysfunction. *Nat. Rev. Neurosci.* 16, 55–61. <https://doi.org/10.1038/nrn3857>.
79. Shepherd, A.M., Matheson, S.L., Laurens, K.R., Carr, V.J., and Green, M.J. (2012). Systematic meta-analysis of insula volume in schizophrenia. *Biol. Psychiatr.* 72, 775–784. <https://doi.org/10.1016/j.biopsych.2012.04.020>.

80. Aschauer, D.F., Kreuz, S., and Rumpel, S. (2013). Analysis of transduction efficiency, tropism and axonal transport of AAV serotypes 1, 2, 5, 6, 8 and 9 in the mouse brain. *PLoS One* 8, e76310. <https://doi.org/10.1371/journal.pone.0076310>.
81. Challis, R.C., Ravindra Kumar, S., Chen, X., Goertsen, D., Coughlin, G.M., Hori, A.M., Chuapoco, M.R., Otis, T.S., Miles, T.F., and Gradinaru, V. (2022). Adeno-Associated Virus Toolkit to Target Diverse Brain Cells. *Annu. Rev. Neurosci.* 45, 447–469. <https://doi.org/10.1146/annurev-neuro-111020-100834>.
82. Tsien, J.Z., Chen, D.F., Gerber, D., Tom, C., Mercer, E.H., Anderson, D.J., Mayford, M., Kandel, E.R., and Tonegawa, S. (1996). Subregion- and cell type-restricted gene knockout in mouse brain. *Cell* 87, 1317–1326.
83. Vong, L., Ye, C., Yang, Z., Choi, B., Chua, S., Jr., and Lowell, B.B. (2011). Leptin action on GABAergic neurons prevents obesity and reduces inhibitory tone to POMC neurons. *Neuron* 71, 142–154. <https://doi.org/10.1016/j.neuron.2011.05.028>.
84. Taniguchi, H., He, M., Wu, P., Kim, S., Paik, R., Sugino, K., Kvitsiani, D., Fu, Y., Lu, J., Lin, Y., et al. (2011). A resource of Cre driver lines for genetic targeting of GABAergic neurons in cerebral cortex. *Neuron* 71, 995–1013. <https://doi.org/10.1016/j.neuron.2011.07.026>.
85. Maren, S., De Oca, B., and Fanselow, M.S. (1994). Sex differences in hippocampal long-term potentiation (LTP) and Pavlovian fear conditioning in rats: positive correlation between LTP and contextual learning. *Brain Res.* 661, 25–34. [https://doi.org/10.1016/0006-8993\(94\)91176-2](https://doi.org/10.1016/0006-8993(94)91176-2).
86. Pryce, C.R., Lehmann, J., and Feldon, J. (1999). Effect of sex on fear conditioning is similar for context and discrete CS in Wistar, Lewis and Fischer rat strains. *Pharmacol. Biochem. Behav.* 64, 753–759. [https://doi.org/10.1016/s0091-3057\(99\)00147-1](https://doi.org/10.1016/s0091-3057(99)00147-1).
87. Gruene, T.M., Flick, K., Stefano, A., Shea, S.D., and Shansky, R.M. (2015). Sexually divergent expression of active and passive conditioned fear responses in rats. *eLife* 4, e11352. <https://doi.org/10.7554/eLife.11352>.
88. Choi, J.H., Yu, N.K., Baek, G.C., Bakes, J., Seo, D., Nam, H.J., Baek, S.H., Lim, C.S., Lee, Y.S., and Kaang, B.K. (2014). Optimization of AAV expression cassettes to improve packaging capacity and transgene expression in neurons. *Mol. Brain* 7, 17. <https://doi.org/10.1186/1756-6006-7-17>.
89. Gradinaru, V., Zhang, F., Ramakrishnan, C., Mattis, J., Prakash, R., Diester, I., Goshen, I., Thompson, K.R., and Deisseroth, K. (2010). Molecular and cellular approaches for diversifying and extending optogenetics. *Cell* 141, 154–165. <https://doi.org/10.1016/j.cell.2010.02.037>.
90. Chow, B.Y., Han, X., Dobry, A.S., Qian, X., Chuong, A.S., Li, M., Henniger, M.A., Belfort, G.M., Lin, Y., Monahan, P.E., and Boyden, E.S. (2010). High-performance genetically targetable optical neural silencing by light-driven proton pumps. *Nature* 463, 98–102. <https://doi.org/10.1038/nature08652>.
91. Sparta, D.R., Stamatakis, A.M., Phillips, J.L., Hovelsø, N., van Zessen, R., and Stuber, G.D. (2011). Construction of implantable optical fibers for long-term optogenetic manipulation of neural circuits. *Nat. Protoc.* 7, 12–23. <https://doi.org/10.1038/nprot.2011.413>.
92. Ting, J.T., Daigle, T.L., Chen, Q., and Feng, G. (2014). Acute brain slice methods for adult and aging animals: application of targeted patch clamp analysis and optogenetics. *Methods Mol. Biol.* 1183, 221–242. https://doi.org/10.1007/978-1-4939-1096-0_14.
93. Pennington, Z.T., Dong, Z., Feng, Y., Vetere, L.M., Page-Harley, L., Shuman, T., and Cai, D.J. (2019). ezTrack: An open-source video analysis pipeline for the investigation of animal behavior. *Sci. Rep.* 9, 19979. <https://doi.org/10.1038/s41598-019-56408-9>.
94. Mombelli, E., Osypenko, D., Palchaudhuri, S., Sourmpis, C., Brea, J., Kochubey, O., and Schneggenburger, R. (2024). Auditory stimuli suppress contextual fear responses in safety learning independent of a possible safety meaning. *Front. Behav. Neurosci.* 18, 1415047. <https://doi.org/10.3389/fnbeh.2024.1415047>.
95. Rossant, C., Kadir, S.N., Goodman, D.F.M., Schulman, J., Hunter, M.L.D., Saleem, A.B., Grosmark, A., Belluscio, M., Denfield, G.H., Ecker, A.S., et al. (2016). Spike sorting for large, dense electrode arrays. *Nat. Neurosci.* 19, 634–641. <https://doi.org/10.1038/nn.4268>.
96. Schmitzer-Torbert, N., Jackson, J., Henze, D., Harris, K., and Redish, A.D. (2005). Quantitative measures of cluster quality for use in extracellular recordings. *Neuroscience* 131, 1–11. <https://doi.org/10.1016/j.neuroscience.2004.09.066>.
97. Giovannucci, A., Friedrich, J., Gunn, P., Kalfon, J., Brown, B.L., Koay, S.A., Taxidis, J., Najafi, F., Gauthier, J.L., Zhou, P., et al. (2019). CalmAn an open source tool for scalable calcium imaging data analysis. *eLife* 8, e38173. <https://doi.org/10.7554/eLife.38173>.
98. Pnevmatikakis, E.A., Soudry, D., Gao, Y., Machado, T.A., Merel, J., Pfau, D., Reardon, T., Mu, Y., Lacefield, C., Yang, W., et al. (2016). Simultaneous denoising, deconvolution, and demixing of calcium imaging data. *Neuron* 89, 285–299. <https://doi.org/10.1016/j.neuron.2015.11.037>.
99. Zhou, P., Resendez, S.L., Rodriguez-Romaguera, J., Jimenez, J.C., Neufeld, S.Q., Giovannucci, A., Friedrich, J., Pnevmatikakis, E.A., Stuber, G.D., Hen, R., et al. (2018). Efficient and accurate extraction of in vivo calcium signals from microendoscopic video data. *eLife* 7, e28728. <https://doi.org/10.7554/eLife.28728>.
100. Claudi, F., Tyson, A.L., Petrucco, L., Margrie, T.W., Portugues, R., and Branco, T. (2021). Visualizing anatomically registered data with brainrender. *eLife* 10, e65751. <https://doi.org/10.7554/eLife.65751>.
101. Bankhead, P., Loughrey, M.B., Fernández, J.A., Dombrowski, Y., McArt, D.G., Dunne, P.D., McQuaid, S., Gray, R.T., Murray, L.J., Coleman, H.G., et al. (2017). QuPath: Open source software for digital pathology image analysis. *Sci. Rep.* 7, 16878. <https://doi.org/10.1038/s41598-017-17204-5>.
102. Chiaruttini, N., Burri, O., Haub, P., Guiet, R., Sordet-Dessimoz, J., and Seitz, A. (2022). An Open-Source Whole Slide Image Registration Workflow at Cellular Precision Using Fiji, QuPath and Elastix. *Front Comp Sci-Switz* 3, ARTN.780026. <https://doi.org/10.3389/fcomp.2021.780026>.
103. Baleisyte, A., Schneggenburger, R., and Kochubey, O. (2022). Stimulation of medial amygdala GABA neurons with kinetically different channelrhodopsins yields opposite behavioral outcomes. *Cell Rep.* 39, 110850. <https://doi.org/10.1016/j.celrep.2022.110850>.
104. Aravanis, A.M., Wang, L.P., Zhang, F., Meltzer, L.A., Mogri, M.Z., Schneider, M.B., and Deisseroth, K. (2007). An optical neural interface: in vivo control of rodent motor cortex with integrated fiberoptic and optogenetic technology. *J. Neural. Eng.* 4, S143–S156. <https://doi.org/10.1088/1741-2560/4/3/S02>.
105. Franklin, K.B.J., and Paxinos, G. (2016). *The Mouse Brain in Stereotaxic Coordinates*, 4th edition (Elsevier/Academic Press).

STAR★METHODS

KEY RESOURCES TABLE

REAGENT or RESOURCE	SOURCE	IDENTIFIER
Antibodies		
rabbit anti-RFP antibody	Abcam	RRID:AB_945213
rabbit anti-RFP antibody	Abcam	RRID:AB_777699
mouse anti-CaMKII antibody	Cayman Chemical	RRID:AB_10352211
anti-rabbit Alexa 568 antibody	Thermo Fisher Scientific	RRID:AB_2534017
anti-mouse Alexa 635 antibody	Thermo Fisher Scientific	RRID: AB_2536185
Chemicals, peptides, and recombinant proteins		
gabazine	Abcam	Abcam:ab120042; Sigma:SR95531
tetrodotoxin; TTX	BioTrend	Cat # BN0517
4-aminopyridine; 4-AP	Sigma-Aldrich	Cat #275875
2,3-dioxo-6-nitro-7-sulfamoyl-benzof[<i>f</i>]quinoxaline; NBQX	BioTrend	Cat #332-11666-3
(2R)-amino-5-phosphonopentanoate; AP5	BioTrend	Cat #HY-100714A
Fluoroshield mounting medium with DAPI	Sigma Aldrich	Sigma:F6057-20ML
cholera toxin B, Alexa 488 conjugate	Thermo Fisher Scientific	Cat #C34775
cholera toxin B, Alexa 647 conjugate	Thermo Fisher Scientific	Cat #C34778
Deposited data		
Raw and analyzed data	This study	10.5281/zenodo.14604021
Experimental models: Organisms/strains		
Mouse: CaMKII ^{Cre} : B6.Cg-Tg(Camk2a-cre)T29-1St/J	Tsien et al., 1996 ⁸² ; Jackson Labs	RRID:IMSR_JAX:005359
Mouse: vGluT2 ^{Cre} : B6J.129S6(FVB)-Slc17a6 ^{tm2(cre)LowJ} /MwarJ	Vong et al., 2011 ⁸³ ; Jackson Labs	RRID:IMSR_JAX:028863
Mouse: Ai9 tdTomato reporter: B6.Cg-Gt(ROSA)26Sor ^{tm9(CAG-tdTomato)Hze/J}	Madisen et al., 2010 ⁵⁰ ; Jackson Labs	RRID:IMSR_JAX:007909
Mouse:Etv ^{Cre} : B6(Cg)-Etv1tm1.1(cre/ERT2)Zjh/J	Taniguchi et al., 2011 ⁸⁴ ; Jackson Labs	RRID:IMSR_JAX:013048
Mouse: Scnn1a ^{Cre} : B6; C3-Tg(Scnn1a-cre)3Aibs/J	Madisen et al., 2010 ⁵⁰ ; Jackson Labs	RRID:IMSR_JAX:009613
Mouse: WT: C57Bl6/J	Jackson Labs	RRID:IMSR_JAX:000664
Recombinant DNA		
AAV1:CAG:FLEX:Arch-eGFP	University of North Carolina Vector Core (UNC-VC), Chapel Hill, NC, USA	UNC:Boyden-AAV-CAG-FLEX-Arch-GFP
AAV1:CAG:FLEX:eGFP	University of Zürich, viral vector facility (UZH-VVF), Switzerland	UNC:Boyden-AAV-CAG-FLEX-GFP
AAV1:shortCAG:FLEX:eGFP	UZH-VVF, Switzerland	cat. #v158-1
AAVretro:pmSyn:eBFP-Cre	Addgene, MA, USA	cat. #51507-AAVrg
AAV8:Ef1 α :FLEX:Chronos-eGFP	UNC-VC, Chapel Hill, NC, USA	UNC:Boyden-AAV-Ef1a:FLEX-Chronos-GFP
AAV8:hSyn:FLEX:Chronos-eGFP	UNC-VC, Chapel Hill, NC, USA	UNC:Boyden-AAV-hSyn:FLEX-Chronos-GFP
AAV8:hSyn:Chronos-eGFP	UNC-VC, Chapel Hill, NC, USA	UNC:Boyden-AAV-Syn-Chronos-GFP
AAV8:hSyn:FLEX:GCaMP6m	UZH-VVF, Switzerland	cat. #v290-8
AAV8:hSyn:eNpHR3.0-eYFP	UZH-VVF, Switzerland	cat. #v560-8
AAV8:hSyn:eGFP	Addgene, MA, USA	cat. #50465-AAV8
AAV8:hSyn:FLEX-eGFP	UZH-VVF, Switzerland	cat. #v115-8
AAV8:hSyn:FLEX:Synaptophysin-mCherry-IRES-eGFP	This study	Custom cloning; packaged by the Bertarelli Foundation Gene Therapy Platform Geneva, Switzerland.

(Continued on next page)

Continued

REAGENT or RESOURCE	SOURCE	IDENTIFIER
Software and algorithms		
VideoFreeze	Med Associates Inc	RRID:SCR_014574
ezTrack	https://doi.org/10.1038/s41598-019-56408-9	RRID:SCR_021496
Igor Pro 7	Wavemetrics Inc.	RRID:SCR_000325
Inscopix Data Processing Software	Inscopix Inc.	Inscopix:IDPS
CalmAn	https://doi.org/10.7554/elife.38173	RRID:SCR_021152
GraphPad Prism	http://www.graphpad.com/	RRID:SCR_002798
Brainrender	https://doi.org/10.7554/elife.65751	RRID:SCR_022328
FIJI	http://fiji.sc (Schindelin et al., Nat Methods 2012)	RRID:SCR_002285
ABBA	https://biop.github.io/ijp-imagetoatlas/	RRID:SCR_023857
QuPath	https://doi.org/10.1038/s41598-017-17204-5 ; https://qupath.github.io/	RRID:SCR_018257
Custom Scripts for histological quantification	This study	https://github.com/bmi-lsym/ABBA-QuPath-post_processing
Custom Scripts for histological post-hoc validation	This study	https://github.com/bmi-lsym/Optogenetic_PostHoc_Validator
Other		
stereotaxic frame for small animals	David Kopf Instruments	David Kopf Instruments:Model 942
hydraulic one-axis manipulator	Narishige	MO-10
500 µm/6.1 mm ProView(TM) GRIN lens	Inscopix Inc	Inscopix:1050-004415
600 µm/7.3 mm ProView(TM) GRIN lens	Inscopix Inc	Inscopix:1050-004413
nVoke imaging system	Inscopix Inc	RRID:SCR_023028
nVista imaging system	Inscopix Inc	RRID:SCR_017407
fear conditioning apparatus	Med Associates Inc	RRID:SCR_016928
electric footshock stimulator	Med Associates Inc	Med Associates:ENV-414S
solid-state diode pumped laser 561 nm	Changchun New Industries Optoelectronics Technology (CNI)	CNI:MGL-FN-561-AOM
solid-state diode pumped laser 473 nm	Changchun New Industries Optoelectronics Technology (CNI)	CNI:MBL-FN-473-150mW
vibrating microtome VT1200S	Leica Microsystems	RRID:SCR_020243
patch-clamp amplifier EPC-10/2	HEKA Elektronik	RRID:SCR_018399
fluorescent microscope BX51WI	Olympus	RRID:SCR_018949
high-power LED blue/green	Cree Inc.	Cree:XPEBRY-L1-0000-00P02
LED driver	Mightex Systems	Mightex Systems: BLS-1000-2
slide scanning fluorescent microscope	Olympus	Olympus:VS120-L100; RRID:SCR_018411
slide scanning fluorescent microscope	Olympus	Olympus:VS200; RRID:SCR_024783
sliding microtome Microm HM450	ThermoFisher Scientific	RRID:SCR_015959

EXPERIMENTAL MODEL AND STUDY PARTICIPANTS DETAILS

All experimental procedures with wildtype or genetically modified mice (*Mus musculus*) were approved by the veterinary office of the Canton of Vaud, Switzerland (authorizations VD3518 and VD3518x1). The following transgenic mouse lines were used: 1) *CaMKII*^{Cre} (B6.Cg-Tg(Camk2a-cre)T29-1Stl/J; JAX stock #005359; RRID:IMSR_JAX:005359;⁸²; 2) *Scnn1a*^{Cre} mouse line (B6; C3-Tg(Scnn1a-cre)3A1bs/J; JAX stock #009613; RRID:IMSR_JAX:009613;⁵⁰ 3) *Etv1*^{CreERT2} mouse line, (B6(Cg)-Etv1^{tm1.1(cre/ERT2)Zjh}/J; JAX stock #013048; RRID:IMSR_JAX:013048; ref.⁸⁴; 4) *VGluT2*^{Cre} mouse line, B6J.129S6(FVB)-Slc17a6^{tm2(Cre)Low}/MwarJ; JAX stock #028863; RRID:IMSR_JAX:028863; ref.⁸³. 5) *Rosa26LSL-tdTomato* (B6.Cg-Gt(ROSA)26Sor^{tm9(CAG-tdTomato)Hze}/J; JAX stock #007909;

RRID:IMSR_JAX:007909; also called Ai9 (ref. ⁵⁰) and referred to as “tdT reporter line” here. For some experiments, the *CaMKII*^{Cre} mouse line (Figure 2), the *Scnn1a*^{Cre} mouse line (Figure S1), the *Etv1*^{CreERT2} mouse line (Figure S1), and the *VGlut2*^{Cre} mouse line (Figure 6) were individually crossed with the tdt reporter line, to visualize Cre-expressing neurons by tdTomato fluorescence. C57Bl/6J strain (JAX stock #000664; RRID:IMSR_JAX:000664) was used as wild-type (WT) mice. Each transgenic mouse line was back-crossed to a C57Bl/6J background for usually at least five generations. Fear learning shows sex-specific differences in rodents.^{85–87} Thus, investigating female and male mice without differentiating between them would have increased the variability of the behavioral results. Therefore, we exclusively studied male mice. The mice were 6–7 weeks and 10–11 week old at the time of surgery and fear learning experiments, respectively. Mice were group-housed under a 12/12 h light/dark cycle (lights on at 7 a.m.) with food and water *ad libitum*. One day prior to surgery until the end of the experiment, mice were separated into single cages. Male mice from 1 to 2 cages were randomly assigned to control (eGFP-expressing or saline controls) or effect group (expressing Arch- or halorhodopsin) for the experiments in Figures 4, 5, 6 and S5. None of the other experiments involved a comparison between effect or control groups. For the experiments in Figure 6, a sample size calculation was performed by running a power analysis on previous Results, giving $N=12$ as the group size; the final numbers were slightly larger (see Results). For all other experiments, no *a priori* sample size calculation was performed.

METHOD DETAILS

Plasmid DNA cloning

We constructed a custom vector AAV:hSyn:FLEX:Synaptophysin-mCherry-IRES-eGFP:CW3SL, to drive Cre-dependent expression of Synaptophysin-mCherry as a presynaptic marker, together with eGFP to observe local expression (plasmid “A”). To accommodate the IRES-based vector size to the packaging capacity of AAV, we chose a monomeric mCherry fluorophore as a tag for Synaptophysin, and used a reduced-size 3'UTR sequence known as W3SL (~0.4 kb), consisting of a minimal WPRE3 sequence and SV40 late polyadenylation signal (ref. ⁸⁸, a gift from Bong-Kiun Kaang; Addgene #61463; RRID:Addgene_61463). Vector construction was done using conventional cloning based on PCR amplification and ligation of DNA fragments. We also generated an alternative plasmid (eGFP-IRES-Synaptophysin-mCherry sequence), which, however, showed a lower expression of Synaptophysin-mCherry and was not further used.

Viral vectors

For anterograde labeling of axonal projections (Figures 1A–1I), a custom-cloned vector AAV8:hSyn:FLEX:Synaptophysin-mCherry:IRES:eGFP (200 nL; $2.0 \cdot 10^{13}$ vector genomes [vg]/mL; packaged by Bertarelli Foundation Gene Therapy Platform at EPFL), was injected into the right pInsCx of *CaMKII*^{Cre} mice. To study collateral projections of pInsCx neurons which project to the anterior LA (Figure S3), C57Bl/6J mice were injected with 100 nL of a 1:1 mix of AAVretro:pmSyn:eBFP-Cre ($1.1 \cdot 10^{13}$ vg/ml; Addgene #51507-AAVrg) and 0.5% cholera toxin subunit B solution (CTB-Alexa647; Thermo Fisher Scientific; cat. C34778) into the left anterior LA. In the same surgery, AAV8:hSyn:FLEX:Synaptophysin-mCherry:IRES:eGFP (200 nL; see above) was delivered into the left pInsCx.

For optogenetically assisted circuit mapping (Figure 2), we injected AAV8:EF1 α :FLEX:Chronos-eGFP (200nL; $4.50 \cdot 10^{12}$ vg/ml; UNC-VC) bilaterally into the pInsCx of *CaMKII*^{Cre} \times *tdTomato* mice. For some experiments, AAV8:hSyn:Chronos-eGFP (200nL; $6.50 \cdot 10^{12}$ vg/ml; UNC-VC) was injected either bilaterally, or unilaterally into the pInsCx (see Figures 2K and 2L).

For the *in vivo* Ca²⁺ imaging experiment in the pInsCx (Figure 3), *CaMKII*^{Cre} mice were injected with AAV8:hSyn:FLEX:GCaMP6m (200nL; $3.2 \cdot 10^{12}$ vg/ml; UZH-VVF; cat. v290-1) into the left pInsCx at three locations (ML -4.3 mm; AP -0.7; DV -3.9, -3.6, -3.2 mm). For the imaging experiments in the anterior LA (Figures 4 and S2), *CaMKII*^{Cre} mice were injected into the left anterior LA with AAV8:hSyn:FLEX:GCaMP6m (200nL; $6.4 \cdot 10^{12}$ vg/ml; UZH-VVF; cat. v290-1). Additionally, these mice were bilaterally injected in the pInsCx with either AAV8:hSyn:eNpHR3.0-eYFP (200nL; $7.3 \cdot 10^{12}$ vg/ml; UZH-VVF; cat. v560-8; “halorhodopsin group”), or with 200 nL of phosphate-buffered saline (PBS; control group) in the same surgery.

For optogenetic inhibition of pInsCx axons in the LA (Figure 5), we expressed halorhodopsin (eNphR3.0; ref. ⁸⁹) by injecting AAV8:hSyn:eNpHR3.0-eYFP (250 nL; $3.65 \cdot 10^{12}$ vg/ml; University of Zürich viral vector facility [UZH-VVF], Switzerland; cat. v560-8) bilaterally into the pInsCx of C57Bl/6J mice. Mice in a control group received AAV8:hSyn:eGFP (250nL; $3.65 \cdot 10^{12}$ vg/ml; Addgene, MA, USA; cat. 50465-AAV8).

For optogenetic silencing of the somata of pInsCx principal neurons (Figure S5), archaerhodopsin-3 (Arch; ref. ⁹⁰) was expressed by injecting AAV1:CAG:FLEX:Arch-eGFP (200nL; $2.05 \cdot 10^{12}$ vg/ml; University of North Carolina Chapel Hill vector core [UNC-VC], NC, USA) bilaterally into the pInsCx of *CaMKII*^{Cre} mice. Mice in the control group were injected with either AAV1:CAG:FLEX:eGFP (200nL; $4.4 \cdot 10^{12}$ vg/ml; UNC-VC), or AAV1:shortCAG:FLEX:eGFP (200nL; $4.4 \cdot 10^{12}$ vg/ml; UZH-VVF; cat. v158-1). The same viruses were used for optogenetic silencing of principal neurons in the anterior LA (Figure 6).

Stereotaxic coordinates

For targeting the pInsCx and the anterior LA, we used the following stereotaxic coordinates: pInsCx: ML (medio-lateral) ± 4.2 mm, AP (anterior-posterior) -0.9 mm, DV (dorsoventral) -3.8 mm; anterior LA: ML ± 3.42 mm; AP -1.12 mm, DV -4.45 mm.

Stereotaxic surgery

Stereotaxic injection of viral vectors and implantation of optic fibers (Figures 5, 6 and S5A–S5H) or GRIN lenses (Figures 3, 4 and S2) were performed in 6–7 week old male mice in a single surgery session.²⁴ Briefly, mice were anesthetized with isoflurane in O₂ (3% for induction, 1.5% for maintenance), and their heads were fixed in a stereotaxic apparatus (Model 942, David Kopf Instruments, Tujunga, CA, USA) using non-rupture ear-bars (Zygoma ear cups, Model 921, David Kopf Instruments). A mix of lidocaine and bupivacaine (~50 µL of 1 mg/mL and 1.25 mg/mL, respectively) in 0.9% NaCl saline was injected subcutaneously for local analgesia. The skull was exposed, and small craniotomies were drilled at the specific stereotaxic coordinates for virus injections and implantations. In cases when implantation of optic fibers or a GRIN lens was done, an additional craniotomy served to insert an anchoring micro-screw (Cat#AMS90/1B-100; Antrin Miniature Specialties, Fallbrook, CA, USA). The viral vector suspension was injected using pulled glass pipettes and an oil hydraulic micromanipulator (MO-10, Narishige Group, Tokyo, Japan) at a speed of 100 nL/min; 5 min waiting time before retraction of the pipette was allowed after each injection.

Optic fiber implants for *in vivo* optogenetic experiments were made from a 200 µm core/0.39 NA/230 µm outer diameter optic fiber (FT200EMT; Thorlabs Inc, Newton, NJ, USA) glued inside 1.25 mm diameter ceramic ferrules (CFLC230; Thorlabs) as described.^{24,91} During surgery, the fiber was slowly advanced until the tip reached a position 500 µm above the injection site. For *in vivo* electrophysiology recordings (Figures S5P–S5S), a custom-made optrode (see below) was similarly implanted above the injection site; its ground wire was pre-soldered to an anchoring micro-screw.

For *in vivo* Ca²⁺ imaging in the pInsCx, a GRIN lens (600 µm/7.3 mm ProView integrated lenses; Inscopix Inc., Palo Alto, CA, USA; cat. 1050-004413) was implanted in the pInsCx at a dorsoventral level of DV -3.4 mm. For Ca²⁺ imaging in the anterior LA, a GRIN lens (500 µm/6.1 mm ProView integrated lenses; Inscopix Inc.; cat. 1050-004415) was implanted 100 µm above the virus injection site in the anterior LA. To reduce tissue deformation, a 25G injection needle was first slowly inserted and retracted to mark the track for GRIN lens implantation. The GRIN lens was then lowered with alternating forward (150 µm) and reverse (50 µm) movements to minimize brain tissue deformation.

The skull bones and the outer surfaces of implants were treated with a light-curing adhesive iBond Total Etch (Kulzer GmbH, Hanau, Germany) and embedded in a light-curing dental cement (Tetric EvoFlow, Ivoclar Vivadent, Schaan, Liechtenstein). The outside end of the GRIN lens was sealed using Kwik-Sil (World Precision Instruments, Sarasota, FL, USA). The skin was stitched and overlaid with Betadine ointment; the drinking water was supplemented with 1 mg/mL paracetamol, and the animals were daily monitored for the following 6 days.

Fear learning protocol

Behavioral experiments (Figures 3, 4, 5, 6 and S5A–S5H) were conducted four weeks post-surgery using an auditory cued fear conditioning paradigm. Mice were first habituated to handling and head tethering with the fiber-optic patch cord or with a dummy miniature microscope during 5–6 daily sessions lasting 15 min each. Fear conditioning was conducted on three consecutive days in a fear conditioning chamber (MED-VFC-OPTO-M, Med Associates Inc., Fairfax, VT, USA) under control of VideoFreeze software (Med Associates Inc.) inside a sound-attenuating enclosure (63.5 × 35.5 × 76 cm; NIR-022MD, Med Associates Inc.). The latter was equipped with a speaker and a CMOS camera with a near-infrared filter for continuous video recordings of mouse behavior at 30 fps.

For the habituation session (day 1), fiber-optic patch cords (200 µm core/0.22 NA; Doric Lenses Inc., Quebec, Canada) or a miniature microscope nVista/nVoke (Inscopix Inc.; Figures 3 and 4, respectively), were attached to the ceramic ferrules or to the GRIN lens docking platform, respectively, before placing the mouse in the fear conditioning chamber set-up for the context A (rectangular plexiglass walls, metal grid floor, cleaned with 70% ethanol). Six tone blocks (CS), each consisting of 30 s long 1 Hz trains of tone beeps (100 ms of 7 kHz, 80 dB, 2 ms rise time) were presented at pseudo-random intervals. For the training session (day 2), mice were again connected to the fiber-optic patch cords or the miniature microscope, placed in the same context A, and presented with six pseudo-randomly spaced CS blocks, each followed by an electric footshock (US; 0.6 mA AC, 1 s long) delivered by a shock generator (ENV-414S, Med Associates Inc.). Optogenetic manipulations, when applicable, took place during 3-s periods centered on the footshock presentations of the training session. For the recall session (day 3), mice in optogenetic experiments were *not* connected to fiber-optic patch cords; mice in imaging experiments were connected to the miniature microscope. The mice were placed in the same conditioning chamber, but now set up for context B (semi-circular walls, smooth acrylic floor, cleaned with soap) and re-exposed to four CS blocks.

During optogenetic inhibition experiments with halorhodopsin or Arch (Figures 5, 6 and S5), green light (561 nm) was delivered during the training session for 3 s, starting 1 s before the footshock, using a diode-pumped solid state laser (MGL-FN-561-AOM-100mW; CNI Lasers). Residual light leakage through the AOM module of the laser was prevented by a mechanical shutter (SHB05T; Thorlabs). The laser power was adjusted for each animal to 10 mW at the fiber tip.

In-vivo electrophysiology

Custom-built optrodes were fabricated using an optic fiber (200 µm core/230 µm outer diameter, NA 0.39; FT200EMT; Thorlabs) as described.²⁴ One day before the start of the fear conditioning protocol, the optrode was advanced by ~100–300 µm in the ventral direction using a micro-drive until a target depth for of 3.7 mm DV was reached, while the mouse was under ketamine anesthesia.

The AP-firing activity of pInsCx neurons in freely moving mice was recorded at 40 kHz sampling frequency with a 16-channel amplifier ME16-FAI-mPA and the MC_Rack software (Multi Channel Systems, Reutlingen, Germany). During the training session, 3 s long

laser light pulses (561 nm, 10 mW) were applied starting 1 s before US #1, 3, and 5, to test for the efficiency of Arch-mediated soma silencing ([Figures S5P–S5S](#)).

Miniature - Microscope Ca²⁺-imaging

The nVista system (Insopix Inc) was used to image Ca²⁺ signals of the pInsCx principal neurons in freely moving mice during three subsequent sessions of fear learning ([Figure 3](#)). Using similar imaging parameters, the nVoke system (Insopix Inc⁶⁴) was used to image principal neurons in the anterior LA, and to silence the axons arising from the pInsCx ([Figures 4 and S2](#)). Throughout the behavioral sessions, GCaMP6m fluorescence was continuously imaged at a rate of 30 frames/s using blue EX-LED light (470 nm, nVista; 450 nm, nVoke). The electronic focusing system of the miniature microscopes cycled through three focal planes spaced by 75–100 μm to maximize the number of imaged cells, resulting in an effective imaging frequency of 10 frames/s. Synchronization between the behavioral and the Ca²⁺-imaging video streams was achieved by recording CS and US presentations with the Insopix GPIO TTL inputs. Halorhodopsin expressed by pInsCx axons in the LA was activated by light of the nVoke system (OG-LED; 590–650 nm⁶⁴), switched on for 3 s at full power (10 mW/mm²), preceding the start of the US #1, 3 and 5 by 1 s ([Figure 4](#)).

Slice electrophysiology

Slice electrophysiology was performed 4–5 weeks following the injection of AAV vectors driving the expression of Chronos in the pInsCx ([Figure 2](#)). One mouse at a time was deeply anesthetized with isoflurane (3% in O₂), decapitated, and 300 μm thick coronal brain slices containing the LA were made with a Leica VT1200S vibrating microtome (Leica Microsystems, Wetzlar, Germany). Slicing was done in ice-cold N-methyl-D-glutamine (NMDG) based slicing buffer, containing (in mM): 110 NMDG, 2.5 KCl, 30 NaHCO₃, 1.2 NaH₂PO₄, 20 HEPES, 25 glucose, 5 Na-ascorbate, 2 thiourea, 3 Na-pyruvate, 10 MgCl₂, 0.5 CaCl₂, saturated with carbogen gas (95% O₂/5% CO₂), pH 7.4, adjusted with HCl. All chemicals were from Sigma-Aldrich (Merck KGaA, Darmstadt, Germany), except HEPES, NaCl, KCl (which were from Thermo Fisher Scientific, Waltham, MA, USA), and MgCl₂ (AppliChem, Darmstadt, Germany). Slices were stored for 7 min at 36°C in a chamber containing slicing buffer, and then transferred to a chamber containing carbogen-saturated storage solution (at room temperature), containing (in mM): 92 NaCl, 2.5 KCl, 30 NaHCO₃, 1.2 NaH₂PO₄, 20 HEPES, 25 glucose, 5 Na-ascorbate, 2 thiourea, 3 Na-pyruvate, 2 MgCl₂ and 2 CaCl₂, pH 7.4 (ref. ⁹²). We mainly used slices containing the anterior-most and the second anterior-most region of the LA for recordings (see [Figure 2M](#)). Whole-cell patch-clamp recordings were performed in an extracellular solution containing (in mM): 125 NaCl, 2.5 KCl, 25 NaHCO₃, 1.2 NaH₂PO₄, 25 glucose, 0.4 Na-ascorbate, 3 Myo-Inositol, 2 Na-pyruvate, 1 MgCl₂ and 2 CaCl₂, pH 7.4, saturated with carbogen gas. The patch-clamp recording set-up was equipped with an upright microscope (BX51WI; Olympus, Tokyo, Japan) with a 60×/0.9 NA water-immersion objective (LUMPlanFl, Olympus) and an EPC10 USB double patch-clamp amplifier (HEKA Elektronik GmbH, Reutlingen, Germany).

Optogenetically evoked EPSCs were recorded at room temperature (22°C–24°C). Chronos was activated with a high-power LED (CREE XP-E2, 460 nm; Cree Inc., Durham, NC, USA) custom-coupled into the epifluorescence port of the microscope using a 30 mm cage optic mounting system and focusing lenses (Thorlabs). EPSCs were evoked by 1 ms blue light pulses (~5 mW/mm²) in the presence of the GABA_A receptor antagonist gabazine (SR-95531, 5 μM; Abcam, Cambridge, UK). For the activation of Arch in slice electrophysiology recordings, a 530 nm high-power LED was employed ([Figure S5I-O](#)). The 530 nm LED was also used for excitation of tdTomato in brain slices. Illumination power and timing was controlled by an LED driver (BLS-1000-2, Mightex Systems, Toronto, Canada). The time-course and intensity of the LED light was measured with a fast photodiode (DET36 A/M, Thorlabs) in the illumination light path; the fast photodiode was calibrated using an optical power meter (1918-R with 818-UV detector; NewPort, Irvine, CA, USA) placed under the 60× objective.

For the whole-cell patch clamp recordings in [Figures 2A–2G](#), A Cs⁺-based pipette solution was used, containing (in mM): 140 Cs-gluconate, 10 HEPES, 8 TEA-Cl, 5 Na-phosphocreatine, 4 Mg-ATP, 0.3 Na-GTP, 5 EGTA, pH 7.2 adjusted with CsOH., at 34°C. All other recordings were made using a pipette solution containing (in mM): 145 K-gluconate, 8 KCl, 10 HEPES, 3 Na-phosphocreatine, 4 Mg-ATP, 0.3 Na-GTP, 5 EGTA, pH 7.2 adjusted with KOH.

Histology and immunohistochemistry

For the anatomical experiments and for *post-hoc* histological validation of opsin expression and optic fiber placements, the mice were euthanized by a lethal injection of pentobarbital (150 mg/kg body weight) and transcardially perfused with 4% paraformaldehyde (PFA; Sigma-Aldrich) in PBS. The brains were post-fixed overnight in 4% PFA, then dehydrated in 30% sucrose solution in PBS. Serial coronal brain sections (40 μm) were cut with a freezing sliding microtome HM450 (Thermo Fisher Scientific, Waltham, MA, USA).

For the mapping of output projections using the Synaptophysin-mCherry construct, immunohistochemistry against mCherry was performed with a primary rabbit anti-RFP antibody (ab62341; Abcam; RRID:AB_945213; 1:400 dilution, or ab34771; Abcam; RRID: AB_777699; 1:500 dilution) and a secondary donkey anti-rabbit Alexa 568 antibody (A10042; Thermo Fisher Scientific; RRID: AB_2534017; 1:200 dilution), using free-floating processing of sections. Immunohistochemistry against CaMKII ([Figures 6C and 6D](#)) was performed with a primary monoclonal mouse anti-CaMKII antibody (clone 6G9; 10011437; Cayman Chemical; RRID: AB_10352211; 1:1000 dilution) followed by a secondary goat anti-mouse Alexa 635 antibody (A31575; Thermo Fisher Scientific; RRID:AB_2536185; 1:500 dilution). Brain sections were mounted on Superfrost Plus slides (Thermo Fisher Scientific) and embedded

in Fluoroshield mounting medium containing DAPI (Sigma-Aldrich). The sections were imaged with a slide scanner automated microscope VS120-L100 or VS200 (Olympus) using a 10x/0.4 NA objective.

QUANTIFICATION AND STATISTICAL ANALYSIS

Behavior data analysis

Video recordings of mouse behavior were analyzed using ezTrack software.⁹³ The space above the mouse (containing optic patch cords or the miniature microscope cable) was cropped to minimize movement artifacts. The movement index trace from ezTrack was further analyzed using custom procedures in IgorPro 7 (WaveMetrics Inc., Lake Oswego, OR, USA). The “freezing” state was assigned if the movement value fell below thresholds of 40 or 200 arbitrary units (without or with cable attachment, respectively) for at least 0.5 s. The percent time spent freezing was calculated for each mouse as a time-binned (10 s) binary freezing state trace, and averaged across all mice in one experimental group. The experimenter, who also analyzed the data, was blinded to the assignment of each mouse to the control, or to the test group. In Figures 5, 6 and S5, a correction for tone-driven startle response was applied (see ref. ⁹⁴ for details). This correction led to an increase in CS-driven freezing of <5% in both control and test groups, and was not critical for any of the conclusions.

Data analysis for *in-vivo* unit activity

Raw voltage traces were band-pass filtered (0.6–6 kHz; 4th-order Butterworth filter) and footshock artifacts were blanked by zeroing under manual control, using custom-written routines in IgorPro 7. Negative-amplitude spikes were detected by thresholding (typically set at –3.8 standard deviations); the spike location was determined by the largest event within a tetrode. Individual spike cut-outs (band-pass filtered at 0.3–6 kHz) were subjected to clustering analysis using the MClust toolbox (Dr. David Redish; University of Minnesota, USA) in MATLAB (MathWorks, USA), which applied an unsupervised clustering algorithm KlustaKwik⁹⁵ using the spike valley and the principal components PC1-PC3 as parameters. The clustering quality was manually controlled and occasionally several clusters were fused together if not well separated. The isolation distance (ID) and L-ratio were then computed to control for type I and type II errors⁹⁶; the clusters with ID > 24 and L-ratio < 0.5 were retained for further analysis thus reducing the total number of clusters in the sample from $n = 54$ to 29 in $N = 2$ mice. The clustered data were re-imported into IgorPro for subsequent waveform matching, Z score calculation, and alignments to the stimuli.

Data analysis for slice electrophysiology

Data was exported from the PatchMaster software (HEKA Elektronik), and analyzed in IgorPro 7 (WaveMetrics) using custom scripts. The EPSC amplitudes were quantified from the average of 10 sweeps. The AMPA-EPSC was measured as the peak of the inward current at –70 mV holding potential.

Ca²⁺-imaging data analysis

The initial processing steps were done using the built-in analysis pipeline of the Insopix Data Processing Software (IDPS; Insopix Inc.). This included: 1) deinterleaving of the video by the focal planes; 2) spatial filtering; 3) motion correction; 4) export of the synchronization timestamps. Motion-corrected videos (one per focal plane) were exported as multiplane TIFFs and processed using the automated CalmAn pipeline⁹⁷ for source separation and ROI assignment based on constrained non-negative matrix factorization.^{98,99} The output from CalmAn analysis was imported into IgorPro 7 for further processing using custom routines. Duplicate cells appearing on neighboring focal planes were removed semi-automatically based on the lateral proximity of their centroids and on the cross-correlation of fluorescence traces. The intensity traces for each i^{th} cell ($F_i(t)$), were standardized by converting them to Z score traces as $Z_i(t) = (F_i(t) - \langle F_i(t) \rangle) / \sigma(F_i(t))$; $\langle F_i(t) \rangle$ and $\sigma(F_i(t))$ being, respectively, the global mean and the standard deviation of the i^{th} cell intensity.

For post-hoc quantification of imaged cell location, we used the centroid coordinates of cells in the image plane as identified by CalmAn and the focal plane position (i.e., distance from the GRIN lens) to assign 3D coordinates of each cell in the coordinate system linked to the GRIN lens center. Next, from the post-hoc images of slices covering the lens implantation region, registered to the digital Allen Brain Atlas (see below in Histological Image Analysis), we estimated the coordinates of the lens center in the atlas coordinate space. From these data, the coordinates of each cell were translated into the 3D space of Allen Brain Atlas. Using an open-source Brainrender software,¹⁰⁰ we then determined which cell belonged to which brain region (see Figures 3E, 4D and S2I). Only the cells contained within pInsCx (VISC; Figure 3) or within the anterior LA (Figures 4 and S2) were retained for analysis.

For longitudinal registration of cells across three experimental days, applied to all Ca²⁺ imaging data, we accepted the identity of a cell to be the same if all of the following was true: a) the cell was present during all three days; b) the cell appeared at the same focal plane across days; c) across days, the cell centroids were the nearest neighbors, and inter-centroid distance did not exceed a proximity threshold of 15 μm .

For color-coded plots of Z-scored Ca²⁺ traces, we used averaged excerpts of traces over $n = 6$ footshock presentations (Figure 3), or over $n = 3$ presentations, separately for “light” (US #1, 3, 5) and “no-light” conditions (US #2, 4, 6; Figure 4). The cells were classified as US-onset responders, if they had a time-average Z score > 0.5 in the time period [0; 1] s following the start of the US; a baseline (0.1s up to US start) was subtracted. The cells were classified as US-offset responders, if they had a time-average Z score > 0.5 in

the time period [1; 3.5] s following the start of US, and the cell was not identified as US-onset responder according to the criterion above. In case of US-offset responders, the average baseline Z score calculated during the period [0; 1] s was subtracted.

Histological image analysis

Analysis of Synaptophysin-mCherry positive nerve terminals (Figures 1A–1I and S3) was performed on every second coronal section (80 μm interval) from the prefrontal cortex to the end of the cerebellum. For this, the brain section images from the slide scanner (see above) were imported into QuPath,¹⁰¹ and registered to the reference Allen Mouse Brain Atlas⁴⁹ using the ABBA plugin¹⁰² under FIJI. Automated detection of synaptophysin-mCherry expressing synaptic terminals was then done in QuPath; the data was quantified and averaged across animals using custom Python and IgorPro scripts (<https://github.com/bmi-lsym/ABBA-QuPath-post-processing>).

For post-hoc analyses of construct expression and optic fiber/GRIN lens placements, every section (40 μm interval) of tissue extending $\sim 500 \mu\text{m}$ anterior and posterior from an implant was analyzed. To quantify the brain areas expressing Arch and illuminated by the optic fiber, we developed an analysis tool in Jython for ImageJ (“Optogenetic_PostHoc_Validator”; see https://github.com/bmi-lsym/Optogenetic_PostHoc_Validator and ref.¹⁰³). For this analysis, brain section images were registered to the Allen Mouse Brain Atlas as described above. Arch-eGFP expression was then analyzed by intensity thresholding of eGFP fluorescence; optic fibers were modeled as cylinders with 500 μm long cones of laser light emanating from their tips (Figures S4, S6 and S7; see ref.¹⁰⁴). Finally, the overlap areas were calculated between i) the Arch-eGFP expressing regions, ii) the cross-sections through the light cones, and iii) the brain regions according to the Allen Mouse Brain Atlas. These areas were then summed up across the image stack for each mouse, to yield an estimate of cumulative surface of brain areas covered by optogenetic stimulation for each brain region (Figure S6). These values will depend on the assumption of the brain area that is illuminated and has effective activation of the optogenetic actuator. We assume that this happens within a distance of 500 μm from the fiber tip (see above), which might be a lower-limit estimate of the manipulated brain tissue volume.

For other post-hoc analyses of construct expression (Figure 6C), or to compare alignments between two brain atlases (Figure S1B), vectorized brain atlas maps from the Paxinos mouse brain atlas¹⁰⁵ were fitted to the image by affine transformation using Adobe Illustrator (Adobe, Mountain View, CA, USA).

Statistical analysis

Statistical testing was performed in GraphPad Prism 10 (GraphPad, San Diego, CA, USA). The distribution of the data was tested for normality using a Shapiro-Wilk test. If normality was confirmed, a paired or unpaired version of the two-tailed Student's t-test was used for two-sample datasets. Two-tailed non-parametric tests were used for non-normally distributed data: a Wilcoxon matched-pairs signed-rank test for paired comparisons, or Mann-Whitney U test for unpaired comparisons. In case of more than two comparison groups, we used either one-way ANOVA followed by Bonferroni post-hoc tests, Friedman test, or Kruskal-Wallis test followed by Dunn's post-hoc test for multiple comparisons (for normally or non-normally distributed datasets, respectively). Post-hoc tests were only performed when the main test (ANOVA or Kruskal-Wallis) reported significant group differences ($p < 0.05$). For the datasets influenced by two factors (e.g., group and time), we used a two-way repeated-measures ANOVA (two-way RM ANOVA) separately for each session of the fear conditioning protocol.

The statistical test used for each experiment is stated in the Results along with the statistical test summary (values of test statistics, degrees of freedom, p -values). Additionally, statistical significance is indicated in relevant Figure panels using asterisks according to the convention: n.s. (not significant), $p > 0.05$; $p \leq 0.05$ (*); $p \leq 0.01$ (**); and $p \leq 0.001$ (***)�.